



Tuning selectivity of acetic acid and alcohols by Brønsted and Lewis acid sites in plasma-catalytic CH₄/CO₂ conversion over zeolites

Li Wang^{a,*}, Linhui Fan^a, Yuezhao Wang^a, Qian Chen^b, Yimin Zhu^a, Yanhui Yi^{b,*}

^a College of Environmental Sciences and Engineering, Dalian Maritime University, Dalian, Liaoning 116026, China

^b State Key Laboratory of Fine Chemicals, Frontier Science Center for Smart Materials, School of Chemical Engineering, Dalian University of Technology, Dalian, Liaoning 116024, China

ARTICLE INFO

Keywords:

Plasma catalysis
CO₂ conversion
CH₄ conversion
Acidity
Acetic acid and alcohols

ABSTRACT

Plasma catalysis enables CH₄/CO₂ direct conversion to oxygenates under mild conditions. However, addressing complexity of oxygenate products is the main scientific challenge. Herein, the roles of Brønsted and Lewis acid site (i.e., BAS and LAS) in tuning the selectivity of acetic acid and alcohols have been comparatively investigated for the first time. BAS and LAS are provided by HZSM-5 and 13X zeolites, respectively, and their amounts are adjusted by steam treatment. Results reveal that BAS significantly promotes acetic acid formation, while LAS favors alcohols generation. In addition, Au supported zeolites show that Au³⁺-BAS synergy exhibits potential for acetic acid. *In-situ* FTIR spectra identify the bicarbonate (HCO_{3,ad}) and formate (HCOO_{ad}) to be the primary surface species on BAS and LAS, respectively. Correspondingly, the pathways for acetic acid and methanol production are proposed based on catalyst characterizations and plasma diagnosis. This work opens up zeolite-based catalysts for selective CH₄/CO₂ conversion to oxygenates.

1. Introduction

Methane (CH₄) and carbon dioxide (CO₂) are known greenhouse gases, and their conversion into useful chemicals and fuels offers an attractive route to deliver a sustainable low-carbon economy and carbon-neutral ecosystem. The existing processes for CH₄ and CO₂ utilization, requiring the generation of syngas (CO and H₂) by dry reforming at high temperatures (> 700 °C), followed by converting syngas into methanol at high pressures, are energy intensive. Due to increasing concern about energy and environment issues, there has been tremendous interest in developing new processes for efficient conversion of CH₄ and CO₂. Plasma technology has already been proven to enable the dry reforming step occurred at low temperature, even at room temperature [1–5]. More importantly, the direct conversion of CH₄ and CO₂ into value-added oxygenates has been reported recently, under mild conditions driven by non-thermal plasma [6–10]. However, this one-step process is currently challenged by the complicated oxygenate products, including alcohols (C₁–C₄OH), acids (acetic acid), ketones (acetone), and aldehydes (CH₃CHO).

Features of radical reaction in plasma chemistry, as being the main reason, bring the poor distribution of oxygenates produced from CH₄/CO₂ plasma. Although lots of works have been devoted to optimize the

plasma parameters and reaction conditions [10–23], such as discharge gap, discharge power, CH₄/CO₂ feed ratio, reaction temperature, packing materials, dielectric and electrode type, the selective formation of single oxygenate is still far away from control.

Coupling of non-thermal plasma with catalysts is widely acknowledged to be a promising way to regulate product distribution through the role of catalyst in accelerating desired reactions. Recently, Fulcheri et al. reported that packing Fe/SiO₂ or Co/SiO₂ catalyst into CH₄/CO₂ plasma greatly promoted the formation of oxygenates with selectivity up to 40%, and the selectivity of alcohols reached 35% in the presence of Fe/SiO₂ [24]. Shao and co-workers found that the Ni⁰ in Ni/NF and NiGa/NF showed high total liquid selectivity of ca. 30% with CH₃COOH being the major product, while the Ni²⁺ in NiO/NF improved alcohols formation with ca. 18% selectivity [25]. They also revealed the enhancement of Co⁰ and oxygen vacancy in Co-MgAlO catalysts on CH₃COOH and methanol formation, respectively [26], and the highest selectivity of oxygenate (40%), consisting of methanol, ethanol, propanol, acetic acid, propionic acid, was obtained over the P-CoMgAl/NF catalyst. Different from the role of Ni⁰ mentioned above, Cu⁰ in Cu/5 A was found to be favorable to produce CH₃OH (18.0%), while Fe²⁺ in Fe/5 A favors production of CH₃COOH (7.9%) [27]. Wang et al. investigated the influences of the ZSM-5 supported metal catalysts (Ag, Pt, Pd,

* Corresponding authors.

E-mail addresses: liwang@dlmu.edu.cn (L. Wang), yiyanhui@dlut.edu.cn (Y. Yi).

<https://doi.org/10.1016/j.apcatb.2024.123938>

Received 14 December 2023; Received in revised form 28 February 2024; Accepted 8 March 2024

Available online 11 March 2024

0926-3373/© 2024 Elsevier B.V. All rights reserved.

Re and Ir) on total selectivity of oxygenates and carbon deposition in plasma-catalytic DRM [28]. They found that Pt species and high ratio of weak acidic sites over Pt/UZSM5 catalyst benefit the formation of liquid chemicals with a selectivity up to 60%, including formaldehyde, methanol, ethanol and acetone, but the specific distribution of these oxygenates was not given. Shirazi et al. reported the pathway of methanol formation in the plasma-driven DRM reaction on a crystalline Ni (111) surface by DFT calculations [29]. Mei et al. evaluated activity of γ -Al₂O₃ supported catalysts (Ni, Ag and Pt) in the plasma-driven DRM reaction, and the highest total selectivity of liquid products was achieved to be 14% with 9% alcohols over Ni/ γ -Al₂O₃ catalyst [30]. Liu et al. found the presence of a small amount of methanol, acetic acid and ethanol in the products of plasma-driven DRM reaction over Ni/BN catalysts [31].

Our previous work achieved an oxygenate selectivity of 50–60%, with ca. 40% for acetic acid and 20% for alcohols, over the Cu/ γ -Al₂O₃ packed in a novel DBD reactor with a special water ground electrode [10]. After that, the valence state of Cu, regulated by the supports, i.e., Al(OH)₃, Mg(OH)₂, SiO₂, TiO₂ and HZSM-5, has been found to significantly affect the distribution of oxygenates [32]. Cu⁺ species are favorable to the formation of acetic acid, which could be further enhanced by the synergy of Cu⁺ species and Brønsted acid sites in the Cu/HZSM-5 catalyst. By contrast, Cu²⁺ species are preferable to promote the generation of alcohols, and the Cu/Al(OH)₃ catalyst with the highest Cu²⁺ content exhibits ca. 20% selectivity of alcohols (dominated by methanol). Moreover, optimizing the Cu/Al(OH)₃ catalysts by Cu loadings and calcination temperatures enhanced the selectivity of alcohols to ca. 38% [33]. Interestingly, increasing copper loading causes shift of the predominant alcohols from methanol to ethanol, and the optimal copper loading for producing methanol and ethanol was 5 wt% and 15 wt%, respectively. Besides the supported Cu catalysts, coupling of Ni/HZSM-5 catalyst with DBD plasma has also been investigated recently [34]. The solid ion-exchange (SIE) Ni/HZSM-5 catalyst with Ni content exceeding 1 wt% improves the alcohols generation, which is attributed to stronger NiO-HZSM-5 interaction and Lewis acid site formed by NiO introduction. Differently, the Ni/HZSM-5 catalysts, prepared by liquid ion-exchange (LIE-) and SIE with 1 wt% loading, possess rich Brønsted acid site and Ni²⁺ species related with HZSM-5 framework, exhibiting a relatively high selectivity of acetic acid.

In brief, existing studies all point out the complexity of the produced oxygenates in the plasma catalytic CH₄/CO₂ conversion, i.e., alcohols, acids, ketones and aldehydes. Among these, acetic acid and alcohols have already been identified to be the main products, and methanol is the primary alcohol, followed by ethanol. Even so, current understandings on catalytic active sites for generation of acetic acid and methanol still stay at the initial stage, since only a few supported metal catalysts were tested in this reaction, and these studies mainly focus on the role of metal components. It is worthy to note that, there is very few studies to reveal the role of the acidic sites in plasma-catalytic CH₄/CO₂ conversion to oxygenates. Therefore, the fundamental questions relating to the capacity of acidic sites, i.e., Brønsted acid site (BAS) and Lewis acid site (LAS), in tuning the competitive formation of acetic acid and methanol remain unanswered.

Zeolite is a class of solid materials with abundant and controllable acidic sites. Therefore, in this study, coupling of zeolites with DBD plasma has been performed to investigate the role of acid sites in producing acetic acid and alcohols from the plasma-catalytic CH₄/CO₂ conversion at ~60 °C and atmospheric pressure. BAS and LAS are provided by HZSM-5 and 13X zeolites, respectively, and their amount are regulated by steam treatment. Correlations of acidic sites with acetic acid and alcohols formation have been well clarified, and the pathways for these two oxygenates are proposed based on *in-situ* FTIR and OES diagnostics. In addition, the corresponding Au supported HZSM-5 and 13X catalysts were evaluated in this reaction as well.

2. Experimental

2.1. Catalyst preparation

The commercial HZSM-5 zeolite (SiO₂/Al₂O₃ = 25) and 13X zeolite (SiO₂/Al₂O₃ = 1.7) were both purchased from Nankai University Catalyst Co., Ltd., China. Their acidity was adjusted through exposing HZSM-5 and 13X parent to a high-temperature steam atmosphere. Specifically, 5 g of HZSM-5 was placed into a reactor and heated to 700 °C at a heating rate of 5 °C/min in air, followed by exposure to a steam atmosphere at 700 °C for 3 h, which was realized by a liquid pump at a water flow rate of 3 mL/h. Subsequently, the resulting material was stirred in 0.6 mol/L nitric acid for 5 h, and then filtered and washed with deionized water to neutralize it. Finally, the paste was dried at 120 °C overnight and calcined in air at 540 °C for 4 h. Similarly, the same procedure was employed to adjust the acidity of 13X zeolite, but the difference was to use 550 °C instead of 700 °C. The resulting samples were denoted as HZSM-5-ST and 13X-ST, respectively.

The Au supported catalysts were prepared by incipient wetness impregnation method. The 0.235 g precursor chloroauric acid (HAuCl₄·xH₂O with Au content of 50%) was dissolved in deionized water, followed by adding 6 g support powder under stirring at 80 °C for 5 h. The resulting mixture was filtered, and dried at 80 °C overnight, and finally calcined at 300 °C for 4 h in air condition. The prepared catalysts were denoted as Au/HZSM-5, Au/HZSM-5-ST, Au/13X, Au/13X-ST and Au/S-1, respectively.

2.2. Catalytic test

The conversion of CH₄ and CO₂ was carried out in a dielectric barrier discharge (DBD) catalytic reactor at a reaction temperature of ca. 60 °C and atmospheric pressure, as illustrated in our previous studies [10,32]. Briefly, the DBD reactor consisted of a pair of coaxial glass cylinders with water circulating in the space between the inner and outer cylinders, and two coaxial electrodes. The circulating water served as ground electrode and maintained reaction temperature at ca. 60 °C via a thermostated water bath. The discharge length was 40 mm with a discharge gap of 3 mm, and the catalyst was directly packed into the discharge area. The flow rate of CH₄ and CO₂ with a 1:1 molar ratio was controlled by mass flow controllers at a total flow rate of 40 mL/min. The frequency was fixed at 9 kHz, and the reaction proceeded for 2 h. The cold trap, consisting of anhydrous ethanol and liquid nitrogen, was connected to the exit of the reactor to condense liquid products, which were quantitatively analyzed using a gas chromatograph (Shimadzu GC-2014 C) equipped with a flame ionized detector (FID) and an FFAP column. The gaseous products were analyzed online using the same GC by both a thermal conductivity detector (TCD) and a FID. The change in gas volume before and after the reaction was measured using a flowmeter.

The conversion of CH₄ and CO₂, and the selectivity of gaseous products and liquid products were used as evaluation indicators. The specific calculation equations are shown as follows.

$$X_{\text{CO}_2}(\%) = \frac{\text{moles of CO}_2 \text{ converted}}{\text{moles of initial CO}_2} \times 100\%$$

$$X_{\text{CH}_4}(\%) = \frac{\text{moles of CH}_4 \text{ converted}}{\text{moles of initial CH}_4} \times 100\%$$

$$S_{\text{CO}}(\%) = \frac{\text{moles of CO produced}}{\text{moles of CH}_4 \text{ converted} + \text{moles of CO}_2 \text{ converted}} \times 100\%$$

$$S_{\text{C}_x\text{H}_y}(\%) = \frac{x \times \text{moles of C}_x\text{H}_y \text{ produced}}{\text{moles of CH}_4 \text{ converted} + \text{moles of CO}_2 \text{ converted}} \times 100\%$$

$$S_{\text{Oxygenates}}(\%) = 100\% - (S_{\text{CO}} + S_{\text{C}_x\text{H}_y}) - \text{ca. 10\% carbon deposition}$$

$$S_{\text{CH}_3\text{COOH}}(\%) = \frac{2 \times \text{moles of CH}_3\text{COOH produced}}{\text{moles of total oxygenates produced}} \times S_{\text{Oxygenates}}$$

$$S_{\text{C}_{1-4}\text{OH}}(\%) = \frac{\text{carbon number} \times \text{moles of alcohols produced}}{\text{moles of total oxygenates produced}} \times S_{\text{Oxygenates}}$$

2.3. Catalyst Characterization

The physicochemical properties of the as-prepared catalysts were analyzed by a series of techniques as follows. The crystalline structure of the catalysts was determined by X-ray powder diffraction (XRD) using an X-ray diffractometer (Rigaku D-Max 2400) with $\text{Cu K}\alpha$ radiation ($\lambda = 0.15406 \text{ nm}$). The scanning range was from 5° to 80° (2θ) with a step size of 0.02° at a scanning speed of $10^\circ \text{ min}^{-1}$. High resolution transmission electron microscopy (HRTEM) was used to analyze the particle size and dispersion of Au species in the catalysts using a JEOL-JEM-2100 field emission transmission electron microscope and XFlash 5030 T X-ray spectrometer of Bruker, Germany, and the acceleration voltage was set to 200 kV. The valence state and chemical environment of Au species in the catalysts were revealed by X-ray photoelectron spectroscopy (XPS) using a Thermo ESCALAB Xi+ spectrometer. An Agilent 5110 inductively coupled plasma emission spectrometer (ICP-OES) from Agilent, USA, was used to measure the Au content of the samples. The oxidation state and coordination of Au species were performed using an Agilent UV-550 ultraviolet spectrophotometer (UV-Vis) in combination with an integrating sphere.

The textural properties of catalysts were measured using a TriStar II 3020 physisorption instrument manufactured by Micrometrics, Inc. Prior to the N_2 physisorption measurement, the samples were degassed under a vacuum system of 350°C for 4 h to remove moisture and other impurities inside material. The specific surface areas (Sg) of the samples were calculated using the Brunauer–Emmett–Teller (BET) equation.

The redox properties of the catalysts were investigated by hydrogen temperature-programmed reduction (H_2 -TPR) using a chemisorption instrument (Quantachrome ChemBET 3000, USA). To avoid the aggregation of Au species at high temperatures, the pretreatment temperature of the samples for the H_2 -TPR analysis was controlled at 300°C for 1 h, which was the same as the calcination temperature for Au-based catalysts. TPR analysis was carried out in a H_2/Ar mixture flow (10 vol% H_2 , 120 mL/min) from room temperature to 800°C at a heating rate of 10°C/min . The H_2 concentration in the tail gas, reflecting the H_2 consumption as a function of temperature, was monitored by a TCD detector with a detector current of 130 mA and attenuation of 4.

The acidity of the catalysts, i.e., amount, strength, and type of acid sites, was investigated by NH_3 temperature-programmed desorption (NH_3 -TPD) and Pyridine adsorption FTIR (Py-FTIR). NH_3 -TPD was performed using the same system as H_2 -TPR. The temperature of sample pretreatment for the NH_3 -TPD analysis was controlled at 550°C for 1 h to remove impurities, and then the sample was cooled to 100°C in N_2 flow. Subsequently, the pretreated sample was purged with NH_3 for 1 h at 100°C , followed by purging with He to remove physically adsorbed NH_3 . Finally, the sample was heated to 800°C under the flowing He and the composition of the effluent gas was measured by a TCD detector with a detector current of 130 mA and attenuation of 4. Py-FTIR spectra in absorbance mode were collected with 4 cm^{-1} resolution on a Nicolet 6700 spectrometer equipped with an MCT cryodetector, cooled by liquid nitrogen. All samples were pressed into the form of self-supporting wafers, which were pretreated in a homemade quartz IR cell with CaF_2 windows at 673 K for 4 h under vacuum conditions (10^{-3} Pa). Subsequently, pyridine vapor was exposed to the sample at ambient temperature for 30 min and then the system was outgassed at 200°C for 30 min, followed by cooling down to room temperature for FTIR spectrum measurement. After that, the system was again outgassed at 350°C for 30 min and subsequently cooled down to room temperature for FTIR spectrum collection, to distinguish the acid strength of BAS and LAS in zeolites.

2.4. In-situ FTIR and OES diagnostics

In-situ FTIR measurements were carried out using a FTIR spectrometer (Nicolet iS10, Thermo Scientific), equipped with a rapidly recoverable detector containing heavy hydrogen triethylene glycol salts (DTGS) [35]. The catalyst was pressed into a wafer, which was placed into a DBD IR cell. Then, CH_4/CO_2 mixture (40 mL/min) with 1:1 molar ratio flowed into the DBD IR cell for 1 h, so that a stable IR background spectrum can be collected. Subsequently, the CH_4/CO_2 plasma was triggered at discharge conditions of 9.2 kHz and ca. 9 W. IR spectra were collected in the first minute and then recorded at an interval of 10 minutes until an hour using an OMNIC software.

FTIR spectra of CO_2 adsorption on zeolites in the absence and presence of plasma have been performed using the FTIR spectrometer. The operated procedures consist of zeolite pretreatment, CO_2 adsorption (with or without plasma) and Ar purging. Firstly, zeolite was pre-purged in Ar gas (200 mL/min) for 1 h at room temperature for recording the FTIR background spectrum. Secondly, instead of Ar gas, CO_2 (40 mL/min) flowed through the DBD IR cell, and FTIR spectra for CO_2 adsorption were collected in the absence or presence of plasma (ca. 8 W discharge power). Thirdly, FTIR spectra of purging stage were recorded through turning off CO_2 and turning on Ar gas (200 mL/min). FTIR spectra of each stage was collected at the time of 5, 10, 15, 20, 25 and 30 min using an OMNIC software.

In-situ OES spectra of CH_4/CO_2 plasma were recorded using a Princeton Instruments ICCD spectrometer (SP 2758) with a 300 g/mm grating, through an optical fibre placed close to the ground electrode of the DBD reactor. The slit width of the spectrometer was fixed at $20 \mu\text{m}$ and the exposure time was 2 s.

3. Results and discussion

3.1. Brønsted acid site (BAS) versus acetic acid formation

It is widely accepted that HZSM-5 zeolite is rich in BAS, that originates from the framework aluminium, i.e., H sites in Si-O(H)-Al units. Therefore, BAS in this work is provided by HZSM-5, and its amount are regulated by treating parent HZSM-5 in a steam atmosphere at 700°C , which can cause dealumination from the framework of HZSM-5 [36]. The HZSM-5 sample after steam treatment is denoted as HZSM-5-ST. Besides, S-1 zeolite is used as a reference, since it possesses a similar framework with HZSM-5, but the BAS of S-1 zeolite could be ignored, due to the absence of aluminium on the framework.

Fig. 1 and Table 1 show the characterization results of the employed samples in this work. XRD patterns in Fig. 1(a) reveal that HZSM-5 related samples all exhibit the typical MFI topology, even the ones suffering from high-temperature steam treatment. This is supported by the well-preserved diffraction peaks at $2\theta = 7.8^\circ, 8.8^\circ, 23.1^\circ, 23.9^\circ$ and 24.3° displayed in Figure S1(a), representing the typical (101), (200), (501), (303) and (133) crystal faces of HZSM-5 [37], respectively. However, there are some observed variation in the relative intensities and locations of these diffraction peaks. Steam treatment increases the peak intensities of (101) and (200), but decreases the peak intensities of (501), (303) and (133). Meanwhile, these peaks shift towards higher 2θ value, revealing the contraction of HZSM-5 unit cell caused by steam treatment. Moreover, the framework symmetry of unit cell changes from the orthorhombic symmetry to the monoclinic symmetry after steam treatment, which is identified by the (133) diffraction peak shape [38, 39]. As shown in Figure S1(b), the (133) diffraction peak of the parent HZSM-5 is characteristic of orthorhombic symmetry, which, however, is divided into two peaks for the HZSM-5-ST sample, representing a clear evidence of the monoclinic symmetry. Besides, Au loading has no influence on the framework symmetry, but slightly decreases the diffraction peak intensities of HZSM-5 and HZSM-5-ST, as shown in Figure S1(c) and (d). These changes of XRD patterns point to the removal of Al from the HZSM-5 framework caused by steam treatment, which can also be

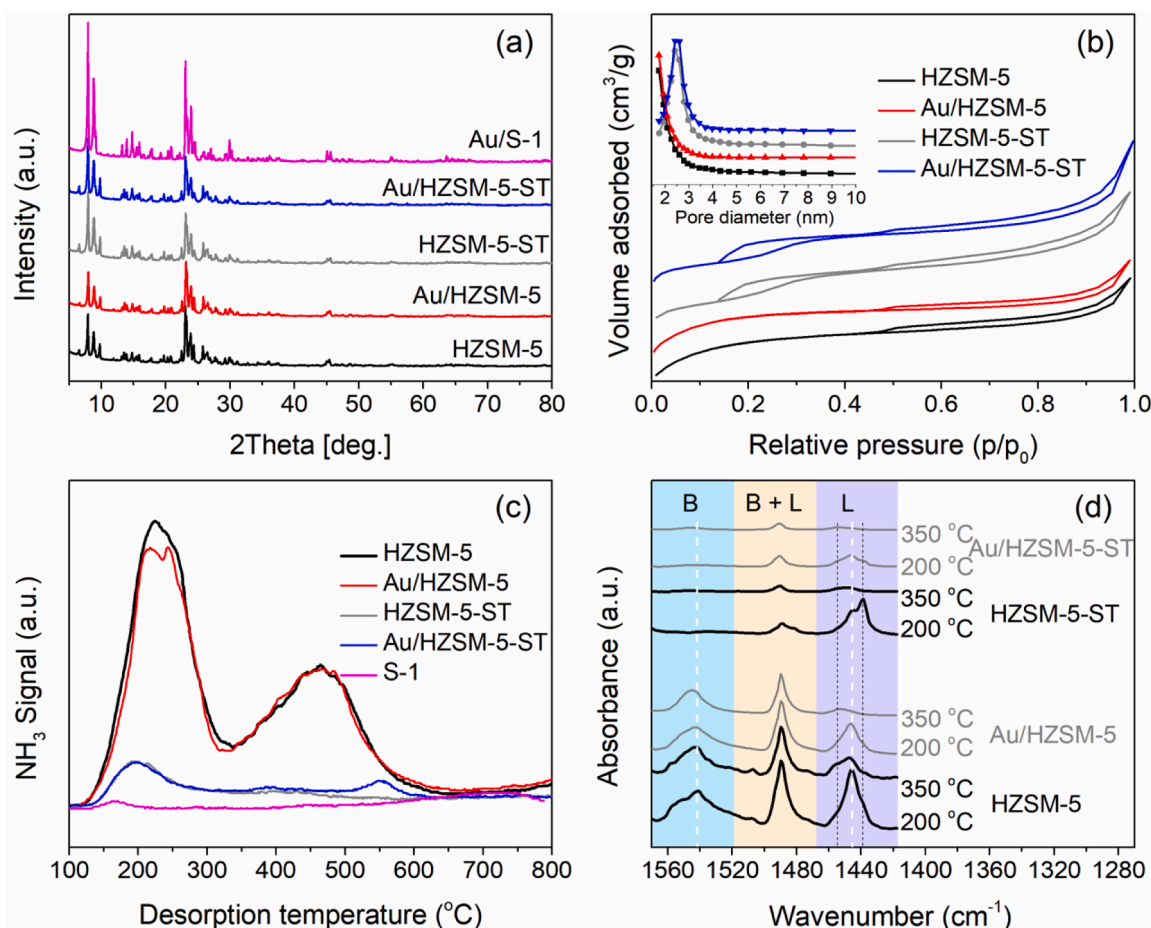


Fig. 1. Characterizations of the HZSM-5, Au/HZSM-5, HZSM-5-ST, Au/HZSM-5-ST and Au/S-1. (a) XRD patterns; (b) N₂ adsorption-desorption isotherms; (c) NH₃-TPD profiles; (d) Py-FTIR spectra. ("ST" represents HZSM-5 suffering from steam treatment at 700 °C).

Table 1

Results of ICP and N₂ physisorption of the HZSM-5, HZSM-5-ST, Au/HZSM-5, Au/HZSM-5-ST and Au/S-1.

Catalyst	Au content (%)	S _{BET} (m ² /g)	S _{EXT} (m ² /g)	S _{MIC} (m ² /g)
HZSM-5	-	399.4	82.3	317.1
HZSM-5-ST	-	361.8	123.7	238.2
Au/HZSM-5	0.036	399.2	70.0	329.2
Au/HZSM-5-ST	0.015	355.9	109.4	246.5
Au/S-1	0.074	421.5	93.6	327.9

supported by the following results of N₂ physisorption, NH₃-TPD and Py-FTIR.

N₂ adsorption-desorption curves are exhibited in Fig. 1(b), it can be seen that HZSM-5 and Au/HZSM-5 both display the isotherms with H4-type hysteresis loops at $0.4 < P/P_0 < 1.0$, indicating the presence of mesopores with a slit-like and irregular shape. The observed mesopores mainly originate from the inter-crystal voids, formed by the aggregation of zeolite crystals, since HZSM-5 is a typical micropore zeolite [40]. By contrast, an extra new hysteresis loop appears in the low pressure range of $0.1 < P/P_0 < 0.4$ for the HZSM-5-ST and Au/HZSM-5-ST, which could be assigned to intracrystalline supermicropores or small mesopores [41, 42]. In this study, the low-pressure hysteresis loop corresponds to small mesopores with a pore size of ca. 2.5 nm, which was mainly created by steam treatment. These variations of pores agree well with the decreased specific surface area (S_{BET}) and micropore surface area (S_{MIC}), but the increased external surface area (S_{EXT}) for the HZSM-5-ST. Therefore, the N₂ physisorption results demonstrate Al extraction from the HZSM-5 framework by steam treatment, which creates the small mesopores.

Figs. 1(c) and 1(d) display the comparative changes in the acidity of samples, evaluated by NH₃-TPD and Py-FTIR, respectively. Clearly, the acidic sites are nearly negligible for the S-1 zeolite. For HZSM-5 and Au/HZSM-5, NH₃-TPD profiles exhibit two desorption peaks in the range of 150–350 °C and 300–600 °C, representing abundant weak and strong acid sites in HZSM-5, respectively. However, the samples after steam treatment (HZSM-5-ST and Au/HZSM-5-ST) show much lower intensity for the peak at 150–350 °C, and negligible peak at 300–600 °C, which means that steam treatment significantly reduces the amount of weak acid sites and almost eliminates the strong acid sites. Furthermore, Py-FTIR is employed to identify the type of these observed acidic sites, i. e., Brønsted acid site (BAS) and Lewis acid site (LAS), as shown in Fig. 1(d). To distinguish the acid strength of BAS and LAS, all samples were recorded at outgassing temperatures of 200 °C and 350 °C, respectively. The IR bands at around 1540, 1445, and 1490 cm⁻¹ are assigned to the vibration of pyridine molecules chemisorbed on BAS, LAS and their joint contributions [39,43], respectively. It can be seen that, the parent HZSM-5 has both BAS and LAS, and the strength of BAS is stronger than that of LAS, since the reduction in intensity of BAS by 350 °C outgassing is less pronounced in comparison with that of LAS. In addition, the parent HZSM-5 displays two shoulder peaks near the LAS peak at 1445 cm⁻¹. The one at 1438 cm⁻¹ is assigned to the 19b mode of gas-phase pyridine [39]. The other one at 1455 cm⁻¹ represents a few LAS with stronger acid strength in comparison with the main LAS (1445 cm⁻¹) [43], because its peak intensity almost unchanged with increase of outgassing temperature from 200 to 350 °C. These findings indicate that the strong BAS and LAS both contribute to the strong acid sites, while the weak acid sites observed in NH₃-TPD of the parent

HZSM-5 in Fig. 1(c) are mainly corresponds to the weak LAS. It is worth to note that, steam treatment leads to disappearance of BAS (1540 cm^{-1}) in HZSM-5, while the main LAS (1445 cm^{-1}) are still appreciable in the HZSM-5-ST. Au/HZSM-5 and Au/HZSM-5-ST show similar conclusions to the corresponding pure zeolites. Combining the XRD, N_2 physisorption and NH_3 -TPD results, it can be reconfirmed that steam treatment results in the removal of framework Al from HZSM-5 structure.

Possible dealumination process of the high-temperature steamed HZSM-5 is depicted in Scheme S1. HZSM-5 consists of a network of TO_4 tetrahedra ($\text{T} = \text{Si}$ or Al) linked by one oxygen, and the bond length of Al-O is longer than that of Si-O [44]. Thus, dealumination starts with breaking of the weak Al-O bond rather than the Si-O bond. When Al-O bond is broken, H_2O binds with the generated tri-coordinated Al, and subsequently hydrolyzes to form an Al-OH species. Similarly, when the second Al-O bond in Al-O-Si unit is broken, another H_2O molecule coordinates to the new formed tri-coordinated Al, and meanwhile a new Si-OH species is formed by binding of the H from H_2O hydrolysis with the $-\text{O-Si}$. Similar process proceeds until the framework Al is entirely dislodged from HZSM-5 structure to form extra-framework Al (EFAl) species, i.e., $\text{Al}(\text{OH})_x \cdot 3\text{H}_2\text{O}$, $x = 3, 2$ and 1 , representing octahedral, penta-coordinated and tetrahedral EFAl [36], respectively. These EFAl species are removed from the steamed HZSM-5 sample by nitric acid leaching and a subsequent washing with deionized water. The remaining tetrahedral Si with two OH unit reorganizes each other to form

Si-O-Si by calcining in air to lose water molecules, which explains the well-preserved MFI topology for the HZSM-5-ST in Fig. 1(a), even the framework Al has been removed from the HZSM-5 framework.

These distinct samples were evaluated in plasma-catalytic CH_4/CO_2 conversion to investigate the influence of BAS on the distribution of oxygenate products, as shown in Fig. 2. Clearly, the liquid product was achieved in addition to the gaseous CO and hydrocarbons (Fig. 2(a)). The produced liquid consists of acetic acid (CH_3COOH), alcohols ($\text{C}_1\text{-C}_4\text{OH}$), acetaldehyde (CH_3CHO) and acetone (CH_3COCH_3), and they are correspondingly denoted as R-COOH , R-OH , R-CHO and R-CO-R , respectively. As shown in Fig. 2(b), the distribution of these oxygenates changes with the employed catalysts. Both HZSM-5 and Au/HZSM-5 exhibit high selectivity toward CH_3COOH , which, however, obviously decreases over the corresponding steam-treated samples (i.e., HZSM-5-ST and Au/HZSM-5-ST). On the contrary, the selectivity of R-OH increases over the steam-treated catalysts. Combining the results achieved in Fig. 1, the decreased CH_3COOH selectivity should be caused by the disappearance of BAS in HZSM-5 during steam treatment, suggesting the positive effect of BAS for acetic acid production. This conclusion can also be applicable to the Au/S-1 catalyst, which shows negligible BAS and low selectivity of CH_3COOH . Therefore, it can be concluded that BAS enhances the production of acetic acid, while disfavors the formation of alcohols.

In addition to BAS, the enhancement of CH_3COOH formation by Au

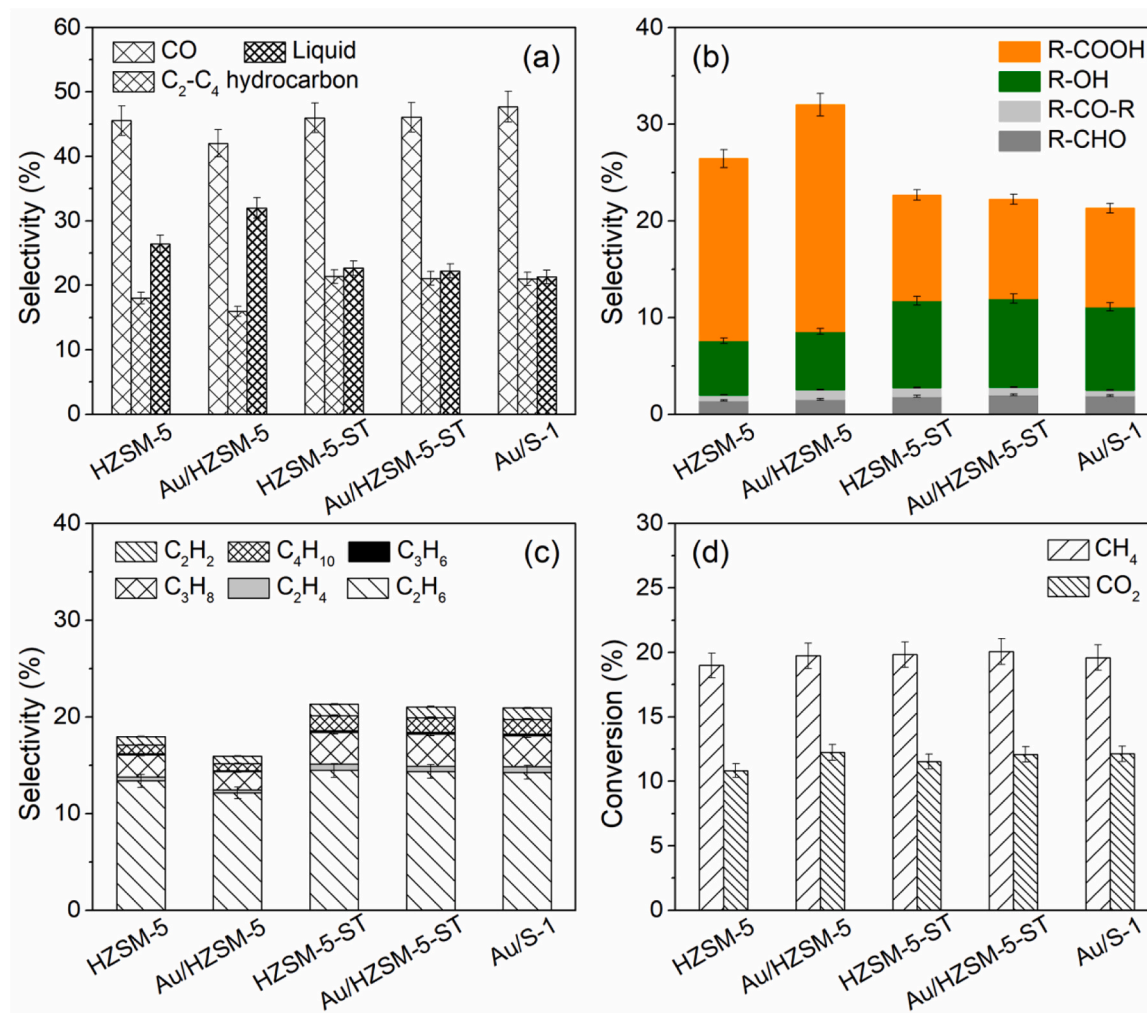


Fig. 2. Catalytic performances of the HZSM-5, Au/HZSM-5, HZSM-5-ST, Au/HZSM-5-ST and Au/S-1 in plasma-catalytic CH_4/CO_2 conversion, to highlight the role of BAS for acetic acid formation. (a) Distribution of product; (b) Selectivity of liquid oxygenates; (c) Selectivity of gas products; (d) Conversion of CH_4 and CO_2 . (discharge power 12 W, discharge frequency 9 kHz, total flow rate 40 mL/min, $\text{CH}_4/\text{CO}_2 = 1:1$, 60°C , 1 atm pressure).

active sites has been observed in Fig. 2. In comparison with the parent HZSM-5, Au/HZSM-5 improves the selectivity of CH_3COOH , while the BAS of HZSM-5 decrease after Au loading (Fig. 1(d)). This reflects that Au has a positive effect on acetic acid generation as well. Thus, the Au-based catalysts have been characterized using ICP, XRD, UV-Vis, XPS, H_2 -TPR and HRTEM, as shown in Table 1, Fig. 3 and Figure S2. ICP analysis shows a very low content of Au in these catalysts, and the highest one (Au/S-1) is lower than 0.1 wt%. Even so, the XRD patterns of these catalysts still show the diffraction peaks of Au at 38.2° in Fig. 3(a), assigned to the (111) lattice plane of metallic Au nanoparticles [45]. However, no apparent Au nanoparticles are observed in the HRTEM images (Figure S2), and the observed interference fringes are ascribed to the HZSM-5. This is probably related to the very low content and poor dispersion of Au species on the HZSM-5 and HZSM-5-ST (Table 1). Even so, the existed metallic Au nanoparticles are further verified by the UV-Vis spectra, as shown in Fig. 3(b). The adsorption peak at ca. 520 nm, assigned to the well-known surface plasmon resonance (SPR) of zero valence gold (Au^0) nanoparticles, is observed for these catalysts [46,47]. However, the intensity of Au^0 SPR is very weak, which may be caused by poor dispersion and big nanoparticles of Au, demonstrating a weak plasmon effect [46,47]. For the Au/HZSM-5, the other two obvious absorption peaks are observed at ca. 267 nm and 357 nm, which are attributed to Au^+ and Au^{3+} , respectively [48]. However, the Au^{3+} species disappears in the Au/HZSM-5-ST, suggesting that Au^{3+} species is closely associated with framework Al. More specifically, the Au^{3+} species originates from the Au-exchanged H^+ sites in Si-O(H)-Al of HZSM-5, because the significant difference between the HZSM-5-ST and HZSM-5

is the framework Al. This result can also be further supported by the absence of Au^{3+} in the Au/S-1 catalyst, which has no framework Al and thus has no exchangeable H^+ sites. XPS spectra (Au 4f7/2) in Fig. 3(c) show no obvious Au signals for these catalysts, revealing that those Au species detected by UV-Vis mainly located inside channels of zeolites, since XPS is only sensitive to the surface species (≤ 10 nm from surface in depth), or it might be related to the very low contents of Au in these catalysts (Table 1). Regarding to significant sensitivity of Au species to temperature, the temperature of pretreatment for the H_2 -TPR analysis was controlled at 300°C , the same as the calcination temperature for these Au catalysts, aiming to avoid the aggregation of Au species at high temperatures. As shown in Fig. 3(d), no H_2 consumption peak was observed for the Au/S-1, which further confirms the metallic state of Au species on the S-1. By contrast with pure HZSM-5, both Au/HZSM-5 and Au/HZSM-5-ST display higher H_2 consumption peaks in the range of $300\text{--}500^\circ\text{C}$, demonstrating existence of Au ion in the two catalysts. Combining the UV-Vis results in Fig. 3(b), the high-temperature peak ($300\text{--}500^\circ\text{C}$) represents the reduction of Au^+ into Au^0 , since the reduction of Au^{3+} to Au^+ was reported to be at a lower temperature, even at room temperature for Au-based zeolites [46,49]. Compared with Au/HZSM-5-ST, Au/HZSM-5 requires a little higher temperature for reduction of Au ion, which can be attributed to the stronger interaction of Au species with the acid sites of HZSM-5 (Fig. 1) [46].

Combining the results shown in Fig. 2, Au/HZSM-5-ST and HZSM-5-ST show a similar distribution of oxygenate products, indicating that Au supported on the HZSM-5-ST does not affect the selectivity of acetic acid. Since Au^+ and Au^0 are the major species in the Au/HZSM-5-ST

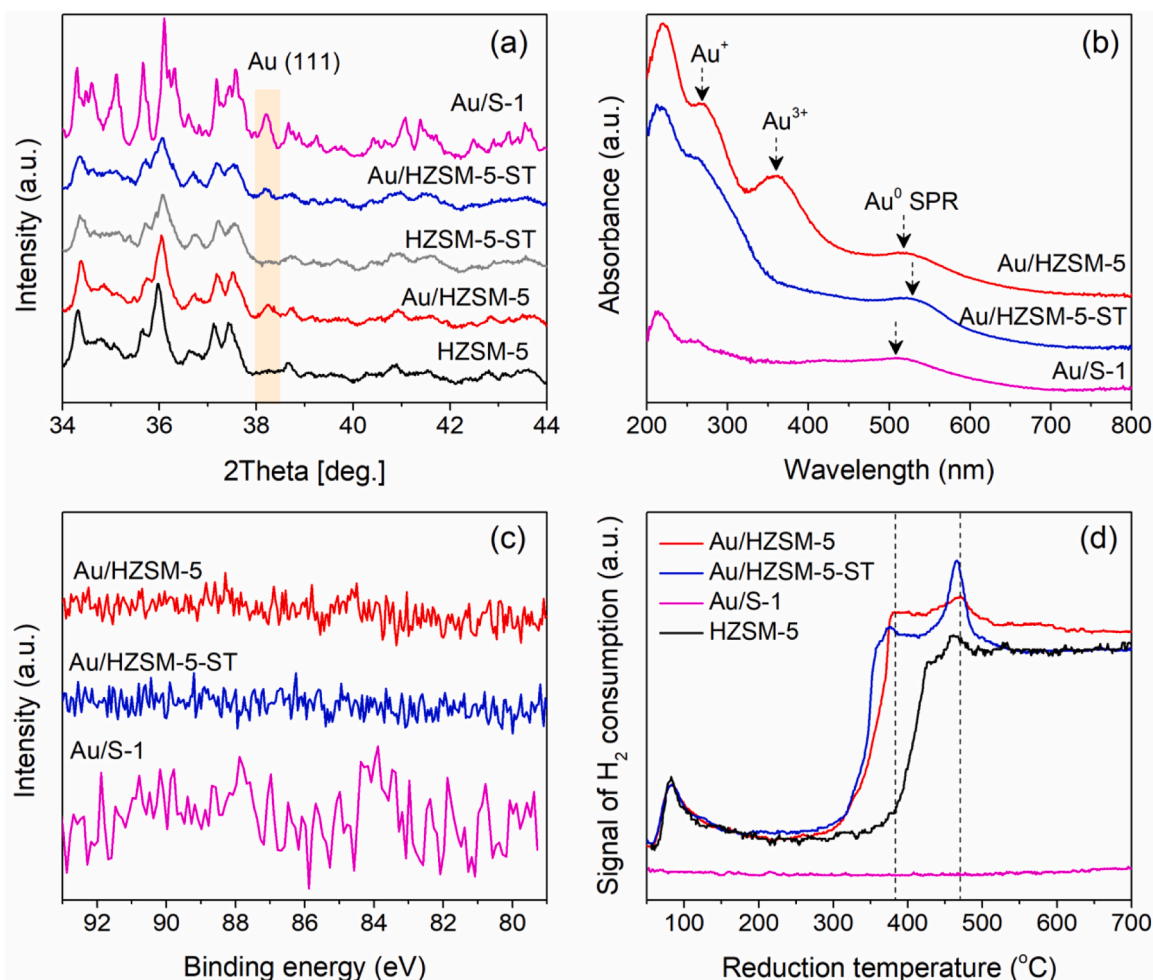


Fig. 3. Characterization of Au species. (a) XRD patterns; (b) UV-Vis spectra; (c) Au 4f7/2 XPS. and (d) H_2 -TPR profiles.

catalyst, the contributions of Au^+ and Au^0 species on acetic acid can be ignored, which can also be supported by the results of Au/S-1. However, different from the Au/HZSM-5-ST, the Au/HZSM-5 not only contains Au^+ and Au^0 species, but also possesses abundant Au^{3+} species, and the Au/HZSM-5 catalyst exhibits the highest selectivity of CH_3COOH , indicating that Au^{3+} species is the dominant Au species for improving the formation of CH_3COOH . Therefore, the synergy of Au^{3+} species with BAS for CH_3COOH production has been achieved experimentally.

3.2. Lewis acid site (LAS) versus alcohols formation

The positive relationship between BAS and acetic acid production has been clarified. However, the relationship between LAS and oxygenates production is still unknown. To get rid of the interference of BAS in clarifying the role of LAS in oxygenates formation, we selected 13X zeolite as the material to provide LAS, as it is a typical zeolite with almost only LAS. Similarly, steam treatment is employed to adjust the LAS in 13X, and the resulting sample is denoted as 13X-ST.

Fig. 4 shows the influence of steam treatment on the physicochemical properties of 13X-based materials. Apparently, both 13X and Au/13X exhibit the typical characteristic peaks of FAU topology, as presented in Fig. 4(a) [50,51]. However, these characteristic peaks almost disappear for the 13X-ST and Au/13X-ST samples. That is, steam treatment causes the collapse of 13X crystal structure, which is also supported by the dramatic decrease in specific surface area from $741.7 \text{ m}^2/\text{g}$ to $28.2 \text{ m}^2/\text{g}$, accompanied by the loss of micropores, as shown in Table 2 and Fig. 4(b). 13X and Au/13X both show isotherms

Table 2

Results of ICP and N_2 physisorption of 13X, 13X-ST, Au/13X and Au/13X-ST.

Catalyst	Au content (%)	S_{BET} (m^2/g)	S_{EXT} (m^2/g)	S_{MIC} (m^2/g)
13X	-	741.7	10.3	731.5
13X-ST	-	28.2	5.2	23.1
Au/13X	0.044	677.2	8.6	668.7
Au/13X-ST	0.063	23.2	2.6	20.6

with Type I and H4 hysteresis loops, which is indicative of microporosity according to the International Union of Pure and Applied Chemistry (IUPAC) classification [40]. By contrast, the hysteresis loops of type IIb are observed for the 13X-ST and Au/13X-ST samples, which indicates the presence of macropores, with typical of no limiting adsorption in the high P/Po region [52]. This finding reveals the collapse of the micropore structure in 13X-ST and Au/13X-ST, which is consistent with the very low crystallinity obtained in Fig. 4(a).

Furthermore, NH_3 -TPD profiles in Fig. 4(c) show that the pure 13X exhibits one broad NH_3 -desorbed peak in the range of $100\text{--}400^\circ\text{C}$ with a small shoulder peak at 350°C , representing abundant weak acid sites and a small amount of medium acid sites, respectively. In comparison with the 13X, similar desorption temperature but a visible increase in the NH_3 -desorbed peak for the weak acid are achieved over the Au/13X catalyst. However, the opposite change is observed for the medium acid sites, which mean that supporting Au on 13X leads to increase in weak acid, but decrease in medium acid. More importantly, these desorption peaks dramatically decrease over the 13X-ST and Au/13X-ST, pointing

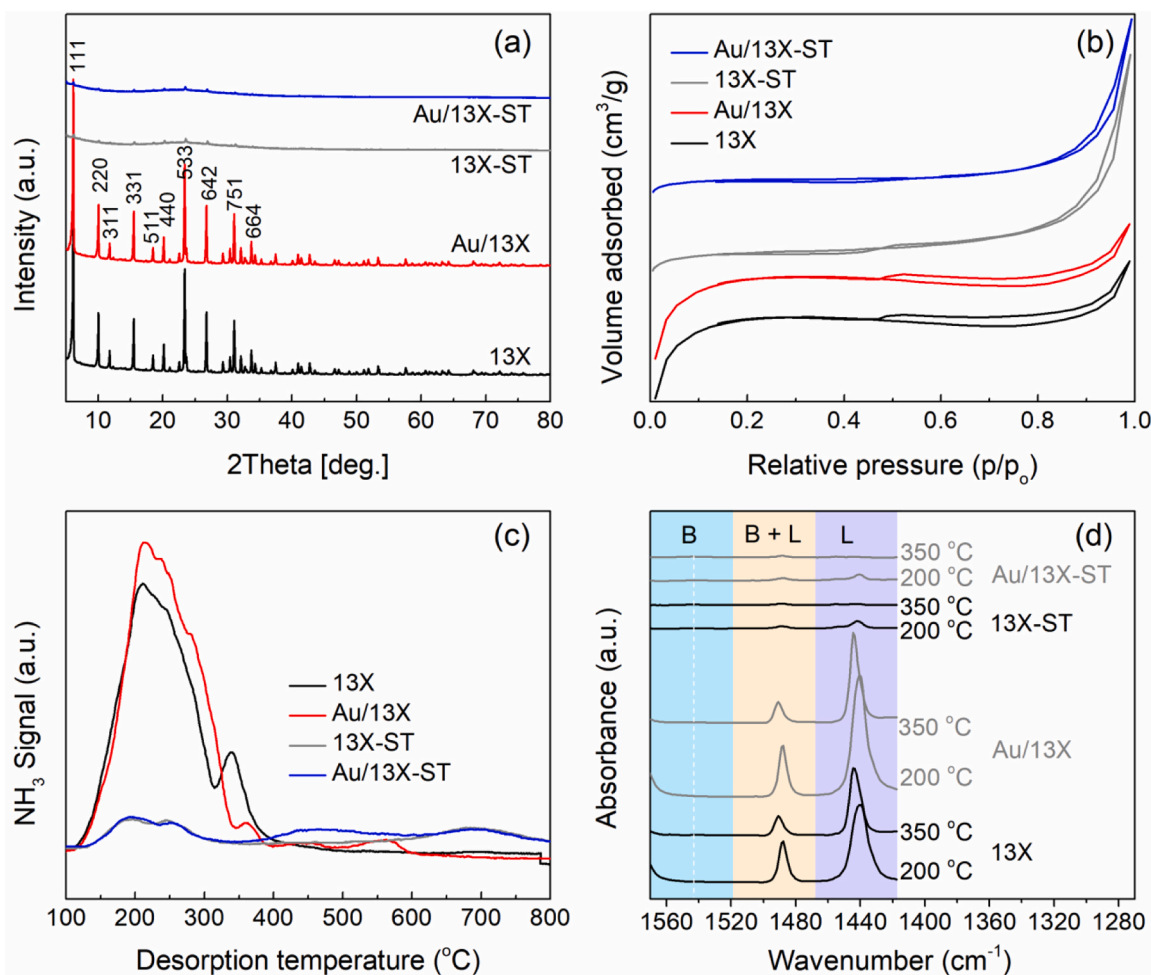


Fig. 4. Characterization of the 13X, Au/13X, 13X-ST and Au/13X-ST. (a) XRD patterns; (b) N_2 adsorption-desorption isotherms; (c) NH_3 -TPD profiles; (d) Py-FTIR spectra. ("ST" represents 13X suffering from steam treatment at 550°C).

out that steam treatment obviously eliminates the acid sites of 13X zeolite by removing framework Al, as framework Al centers are the source of acid sites in zeolites.

Py-FTIR spectra in Fig. 4(d) display an IR band at 1441 cm^{-1} , assigned to the 19b mode of adsorbed pyridine, which is slightly shifted up with respect to liquid pyridine value of 1438 cm^{-1} [53]. This result suggests interactions of pyridine with weak electron-withdrawing sites, which agrees well with the abundant weak acid sites of 13X observed by NH_3 -TPD. In addition, the peak corresponding to BAS (1540 cm^{-1}) does not appear, reflecting no BAS in 13X. That is, pyridine dominantly adsorbs on weakly Lewis acidic Na^+ in 13X. Besides, 350°C outgassing enables the 19b mode diminished in intensity and its maximum frequency shifts up to 1444 cm^{-1} . Notably, steam treatment leads to almost disappearance of LAS, as seen from Py-FTIR spectrum and NH_3 -TPD profile of 13X-ST. Similar phenomena are observed for the Au/13X-ST. In a word, there are abundant LAS but no BAS on 13X and Au/13X. On 13X-ST and Au/13X-ST, however, there is only a very small amount of LAS.

The above-mentioned typical samples, i.e., 13X, Au/13X, 13X-ST and Au/13X-ST, have been tested in plasma-catalytic CH_4/CO_2 conversion to investigate the influence of LAS on the distribution of oxygenates products. As presented in Fig. 5, 13X and Au/13X with only LAS exhibit high R-OH selectivity, which means that LAS promote R-OH production. This is totally different from BAS, that significantly favors R-COOH generation, as concluded in Section 3.1. Additionally, the enhancement of LAS on R-OH formation can be further confirmed by comparing 13X with 13X-ST. They both have only LAS, but the 13X with a much higher

amount of LAS exhibits higher R-OH selectivity than the 13X-ST. By contrast, the selectivity of R-COOH has hardly changed. These findings reveal that LAS significantly improves R-OH generation, but has almost no effect on the formation of CH_3COOH .

In addition, the Au/13X exhibits a similar R-OH selectivity to the 13X, but improves the acetic acid selectivity. Such a phenomenon is also observed when comparing 13X-ST with Au/13X-ST in Fig. 5(b). These results further demonstrate the role of Au in promoting CH_3COOH production. Characterizations of Au/13X and Au/13X-ST catalysts are comparatively displayed in Table 2, Fig. 6 and Figure S3. ICP analysis shows the low content of Au ($< 0.1\text{ wt}\%$) in these two catalysts. HRTEM images in Figure S3 show that only a few Au nanoparticles are observed on the 13X and 13X-ST, and the corresponding particle sizes of Au are about 10 nm. Different from the Au/13X, some Au nanoparticles with irregular shapes, such as triangular and rhomboid nanoparticles, appear on the Au/13X-ST in addition to the spherical nanoparticles, indicating that the steam treatment affects the morphology of Au nanoparticles on 13X. However, the lattice spacing analysis reveals that the exposed lattice planes are all the (111) and (200) planes of metallic Au nanoparticles, regardless of the morphology of Au nanoparticles (Figure S3). In addition to the Au^0 , the Au^+ and Au^{3+} species are observed by XPS and UV-Vis analysis as well. As presented in Fig. 6(a), compared with the Au/13X, the 13X-ST greatly enhances the content of Au^+ species but decreases the amount of Au^0 . Moreover, Au/13X shows the weak absorption peak of Au^{3+} at ca 360 nm, which can be supported by the XPS results presented in Fig. 6(b). The binding energies of Au 4f7/2 at 84.0, 84.6 and 85.9 eV are assigned to metallic Au^0 nanoparticles, Au^+ and

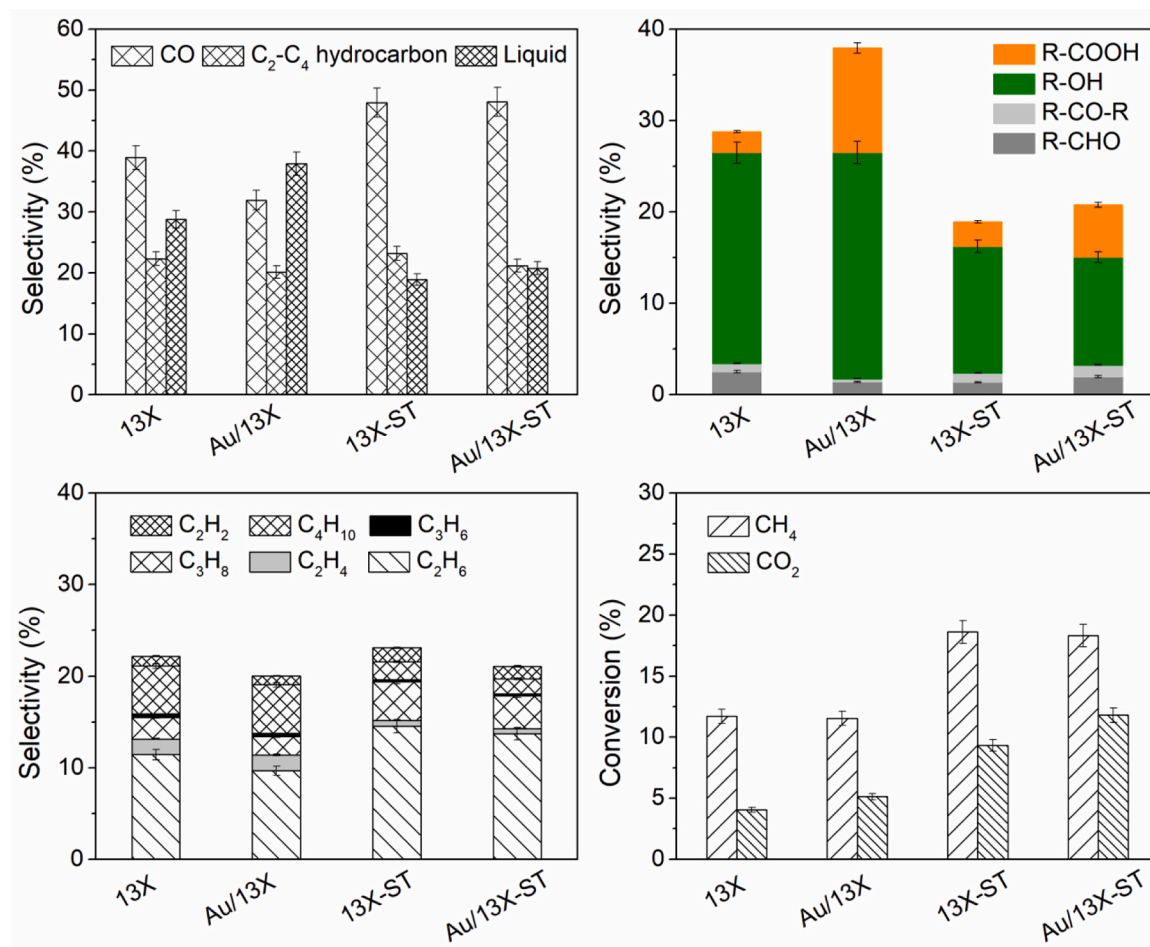


Fig. 5. Catalytic performances of the 13X, Au/13X, 13X-ST and Au/13X-ST in plasma-catalytic CH_4/CO_2 conversion, to highlight the role of LAS for alcohols formation. (a) Distribution of product; (b) Selectivity of liquid oxygenates; (c) Selectivity of gas products; (d) Conversion of CH_4 and CO_2 . (Reaction conditions are the same as Fig. 1).

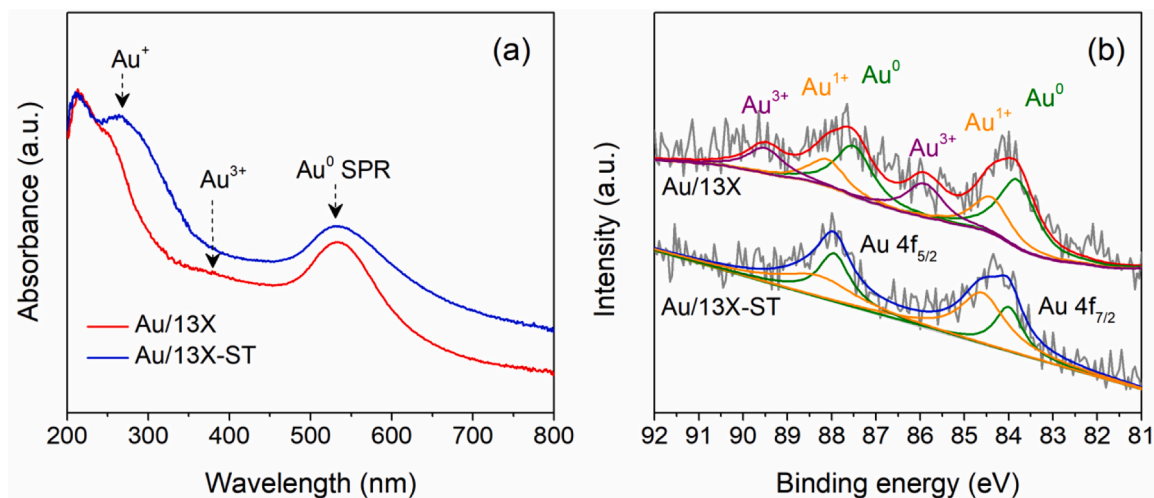


Fig. 6. UV-Vis spectra (a) and Au 4f7/2 XPS (b) of Au species in Au/13X and Au/13X-ST.

Au^{3+} cation species, respectively [46,48]. Apparently, the Au 4f core levels of Au/13X contained Au^0 , Au^+ and Au^{3+} species. By contrast, Au^{3+} is absent in Au/13X-ST, which has more Au^+ species than Au/13X. Combined with the reaction performances of Au/13X and Au/13X-ST, the CH_3COOH selectivity over Au/13X is higher than that over Au/13X-ST, which confirms the enhancement of Au^{3+} on the generation

of CH_3COOH again, in consistent with the results in the case of Au/HZSM-5.

3.3. Surface species on BAS and LAS identified by in-situ FTIR

To reveal the roles of BAS and LAS in tuning the formation of

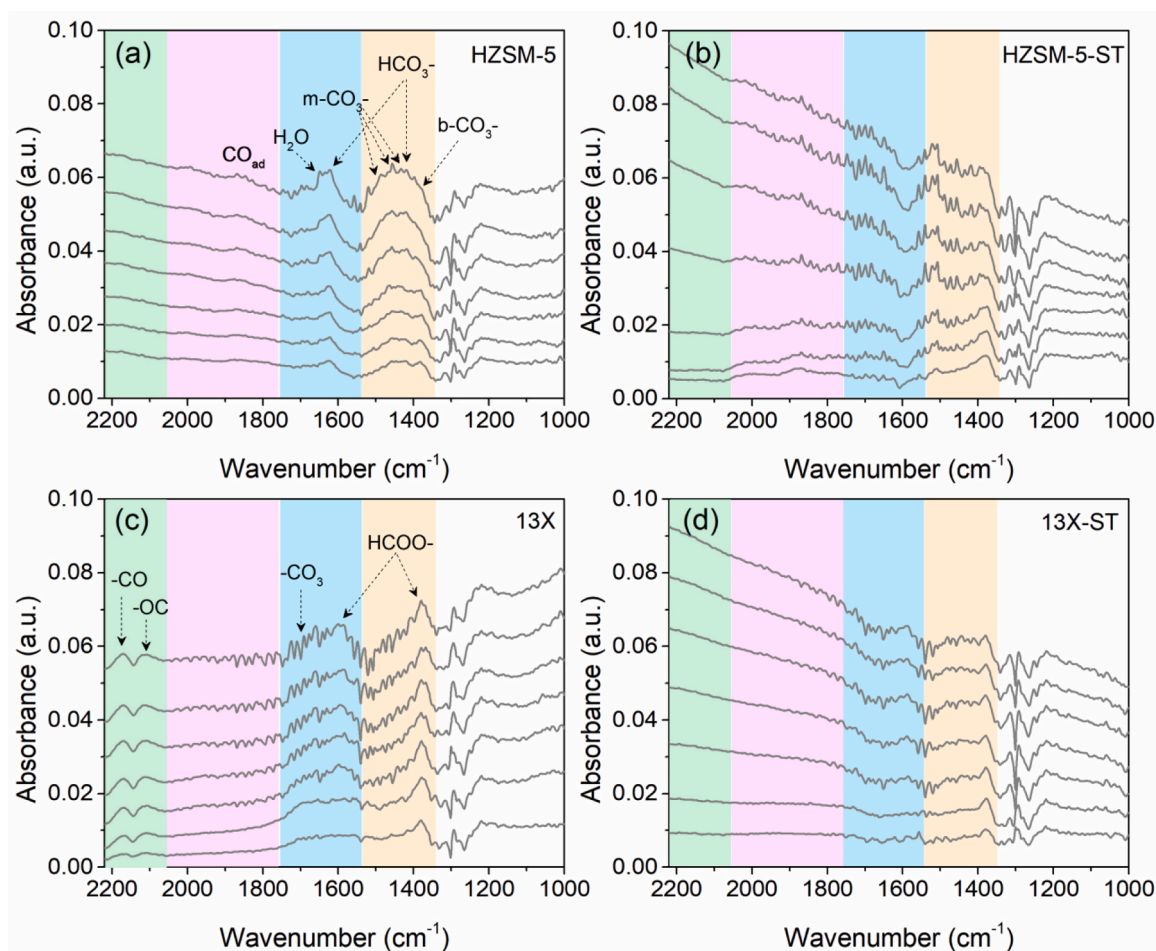


Fig. 7. In-situ FTIR spectra (transmission mode) of plasma-catalytic CH_4/CO_2 conversion employing different zeolites. (a) HZSM-5; (b) HZSM-5-ST; (c) 13X; (d) 13X-ST. (40 mL/min of CH_4/CO_2 mixture with 1:1 molar ratio flowed through the DBD IR cell, and in-situ FTIR spectra were collected at the reaction time of 1, 10, 20, 30, 40, 50 and 60 min from down to up).

CH₃COOH and alcohols, *in-situ* FTIR was employed to identify the surface species formed on HZSM-5 and 13X during the plasma-catalytic CH₄/CO₂ conversion, as presented in Fig. 7. In the case of HZSM-5, a broad absorption band from 1340 to 1540 cm⁻¹ is clearly observed, but poorly resolved, which consists of several species. IR peaks at ca. 1625, 1425 and 1222 cm⁻¹ are assigned to vibrations of surface bicarbonate species (HCO₃-) [54]. IR peaks at ca. 1380 and 1360 cm⁻¹ are attributed to bidentate carbonates (b-CO₃) [53], and the others, appearing at 1485 and 1432 cm⁻¹, as well as 1454 cm⁻¹, normally represent monodentate carbonates (m-CO₃-) [55]. These peaks become intense with reaction time. By contrast with HZSM-5, steam treatment enables HCO₃- almost vanished, while b-CO₃ and m-CO₃ reduced on the HZSM-5-ST in Fig. 7 (b), which is closely consistent with the disappearance of BAS and decrease of LAS in the HZSM-5-ST concluded in Fig. 1. These results indicate that HCO₃- are highly possible formed on BAS, while b-CO₃- and m-CO₃- are probably formed on LAS in HZSM-5. Combining with the performances presented in Fig. 2, it reveals that the role of BAS in HZSM-5 is to activate CO₂ into the HCO₃- species, that is mainly responsible for CH₃COOH production in plasma-catalytic CH₄/CO₂ conversion on HZSM-5 zeolite.

By contrast, the *in-situ* FTIR spectra of 13X are significantly different from those of the HZSM-5, as presented in Fig. 7(c). The dominant absorption bands at 1590 and 1380 cm⁻¹ are assigned to the formate surface species (HCOO-) [54]. A couple of IR bands appear at ca. 2170 and 2113 cm⁻¹, corresponding to CO stretching vibrations, which, however, are absent in the spectra of the HZSM-5. The band at 2170 cm⁻¹ is certainly due to CO interacting through the C atom with Na⁺ in 13X, i.e., C-bonded CO species (Na⁺.....CO), while the band at 2113 cm⁻¹ can be attributed to O-bonded CO species (Na⁺.....OC) [53]. Besides, the band at ca. 1707 cm⁻¹ are normally accepted to be the carbonate-like specie (-CO₃), which is produced by the interaction of the basic framework O in 13X with the C of CO₂ [56]. Notably, in the spectra of 13X-ST, the adsorbed CO and -CO₃ species do not appear, but a small part of HCOO- species remain, as presented in Fig. 7(d). The remaining HCOO- species may originate from its adsorption on the LAS produced by the residual framework of 13X-ST (Fig. 4(a)). These findings further confirm that the observed surface species are closely related with the framework of 13X. Through correlating reaction performances and characterization results, the primary role of LAS in 13X is highly possible to form the HCOO- surface species, which could be the key intermediate for production of alcohols in plasma-catalytic CH₄/CO₂ conversion on 13X zeolite.

3.4. Pathways proposed for acetic acid and methanol generation

Different from thermal catalysis, reaction pathways in plasma catalysis are generally accepted to be related with both gaseous intermediates and surface species. Herein, *in-situ* OES was employed to identify the gaseous intermediates generated in the CH₄/CO₂ plasma packed with different zeolites, as shown in Fig. 8. Clearly, CH, H_α and O radicals, excited-state CO and C₂ are detected when the CH₄/CO₂ plasma was packed by HZSM-5 [10,57]. Besides, abundant excited-state CO₂ (CO₂^{*}) are generated by impacting with free electron in plasma, which has been demonstrated by plasma simulation in our previous study [10]. As for CH radical, the CH₄/CO₂ plasma packed by HZSM-5 shows much higher intensity than that packed by 13X, indicating that much more CH₃ radicals were produced when the CH₄/CO₂ plasma was packed by HZSM-5, based on the simulation results reported by De Bie et al. [58]. This finding is consistent with the achieved higher CH₄ conversion on HZSM-5, that is almost twice as that on 13X, as shown in Figs. 2 and 5. Interestingly, in the case of packing 13X, the intensity of the bands from excited-state CO is extremely low (Fig. 8(b)), however, the adsorbed CO species are clearly identified on the surface of 13X by *in-situ* FTIR spectra (Fig. 7). These results suggest that the CO produced in the CH₄/CO₂ plasma dominantly exits in its ground state [59], and then immediately adsorbs on 13X, instead of being further transformed into excited-state CO by electron impact. On the contrary, the excited state is the primary form of CO produced in the CH₄/CO₂ plasma packed with HZSM-5 [59], as supported by Figs. 7 and 8. Similar phenomena are also observed for the H_α radicals in Fig. 8, by comparing the cases of packing CH₄/CO₂ plasma by HZSM-5 and 13X, respectively.

According to the surface and gaseous species identified by *in-situ* FTIR and OES, the reaction pathways for acetic acid and methanol generation, two major oxygenate products in CH₄/CO₂ plasma, have been proposed, as shown in Figs. 9 and 10, respectively. In the case of packing HZSM-5 into CH₄/CO₂ plasma, the BAS in HZSM-5 significantly enhances the formation of acetic acid (Figs. 1 and 2). As presented in Fig. 9, the BAS in the form of Si-O(H)-Al unit mainly activates the CO₂^{*} produced in plasma to form bicarbonate (-HCO₃) by protonation (Fig. 7). CO₂ protonation over HZSM-5 has already been predicted by DFT calculations in heterogeneous catalysis [60]. In addition, CO₂ adsorption experiments also confirm that CO₂ can adsorb on HZSM-5 to form bicarbonate even in the absence of plasma (Figure S4) [61–64], and when turning on plasma, the corresponding adsorption of CO₂ is strengthened on the HZSM-5. This is mainly attributed to the generated CO₂^{*} with high internal energy, that enables the adsorption and subsequent protonation processes to proceed more easily, in comparison with the ground-state CO₂. The enhancement of excited-state molecules on a

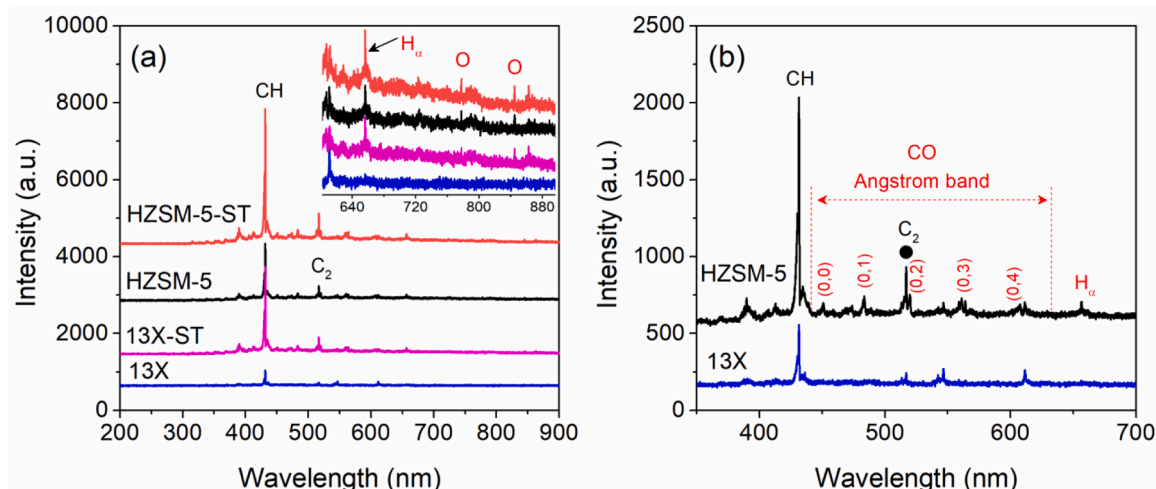


Fig. 8. *In-situ* OES spectra of the CH₄/CO₂ plasma packed with different catalysts.

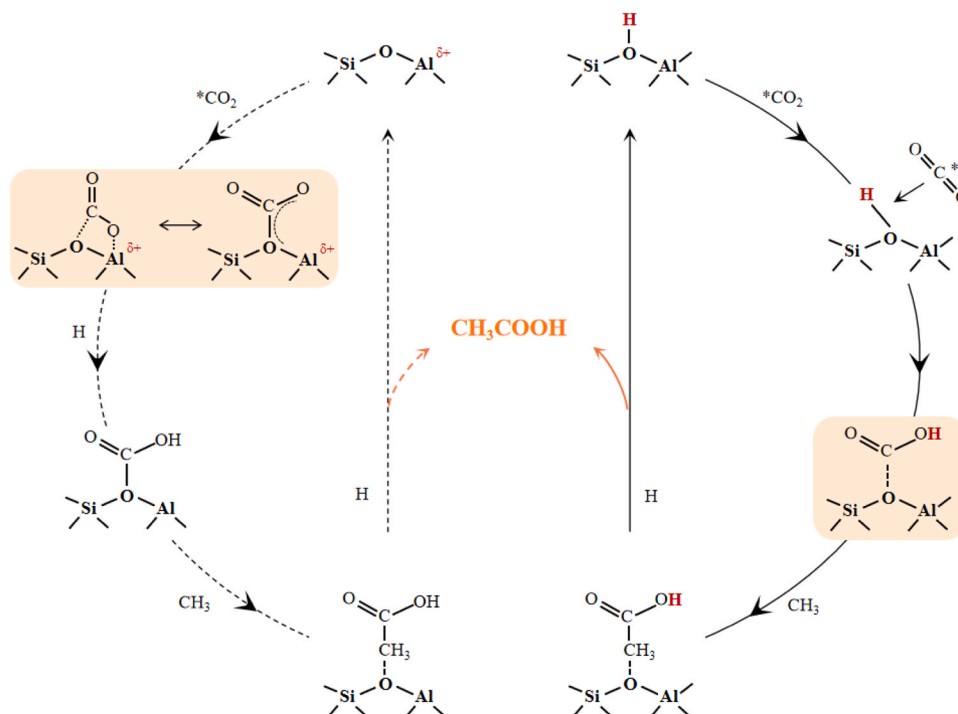


Fig. 9. Reaction pathways for acetic acid formation over BAS in plasma-catalytic CH_4/CO_2 conversion on HZSM-5 zeolite.

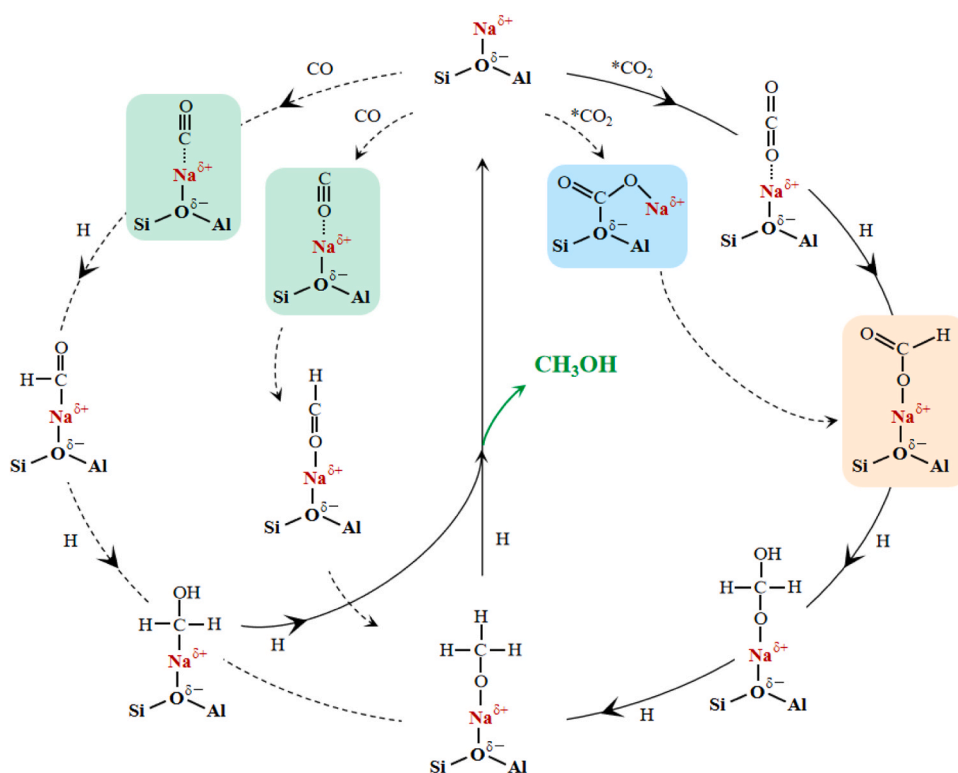


Fig. 10. Reaction pathways for methanol formation over LAS in plasma-catalytic CH_4/CO_2 conversion on 13X zeolite.

catalytic process has been experimentally testified in our previous studies [10,65,66]. Subsequently, the abundant CH_3 radicals in plasma (Fig. 8) could attack the C-O bond of $-\text{HCO}_3$ to form $-\text{CH}_3\text{COOH}$ species, which finally reacts with the active H radicals in plasma to produce CH_3COOH through Eley-Rideal (E-R) process [67]. Meanwhile, the BAS is regenerated by H radicals from CH_4 splitting. Clearly, this pathway for

producing CH_3COOH strongly depends on the amount of BAS in HZSM-5. That is, the more BAS, the more acetic acid can be formed. This is well supported by the experimental results achieved on HZSM-5 and HZSM-5-ST (Fig. 2).

In addition, the HZSM-5 also contains LAS (Fig. 1), and the possible reaction pathways for acetic acid formation on LAS are proposed in

Fig. 9. Based on the results obtained in Figs. 1, 2, 7 and 8, the CO_2^* could also adsorb on LAS, in addition to BAS, to form the surface carbonate species (Fig. 7). Subsequently, these species could react with H radicals to produce $-\text{HCO}_3$, followed by reacting with CH_3 , and then with H radicals to produce CH_3COOH by E-R processes.

Alcohols (dominated by methanol) are preferentially generated when the 13X was employed instead of HZSM-5, and correspondingly the formate (HCOO^-) has been identified to be the major surface species on the 13X (Figs. 4, 5 and 7). It should be emphasized again that, LAS is the only acidic site in 13X, while BAS is the major one in HZSM-5, and they determine the formation of alcohols and acetic acid, respectively. FTIR spectra of CO_2 adsorption in Figure S5 reveal that CO_2 can adsorb on the parent 13X, which confirms the importance of LAS in the surface reaction on 13X. As shown in Fig. 10, the Na^+ in the $\text{Si-O}(\text{Na})\text{-Al}$ unit provides the LAS in 13X, so it can adsorb the CO_2^* to form linear and carbonate-like specie (Fig. 7) [56]. These species could react with H radicals to produce HCOO^- (Fig. 7), that subsequently undergoes a series of hydrogenation reactions by E-R process [67], and finally methanol is produced and LAS is recovered. In addition to the formate route, the adsorbed CO in Fig. 7 also contributes to methanol generation by multi-step reactions with H radicals, as shown in Fig. 10.

3.5. Role of Au species in plasma-catalytic CH_4/CO_2 conversion

In-situ FTIR spectroscopy has been employed to compare the surface species on Au/HZSM-5 and Au/13X, in comparison with the corresponding parent zeolites. As presented in Figure S6, the Au/HZSM-5 and Au/13X both show similar FTIR spectra to their parent zeolites, indicating that loading Au has limited effects on surface species. This conclusion is supported by the reaction performances shown in Figs. 2 and 5. That is, although Au species shows positive and negative effects toward the generation of acetic acid and CO, respectively, in comparison with the parent HZSM-5 and 13X, this change is not significant, especially for the case of the Au/HZSM-5. There are two possible explanations for the achieved results. Firstly, Au/HZSM-5 and Au/13X both have very low contents of gold, and Au were poorly dispersed on zeolites (Tables 1 and 2, Figures S2 and S3), which limit the catalytic function of Au species. Secondly, in the reaction of catalytic CH_4/CO_2 conversion into acetic acid, metal component is widely accepted to activate CH_4 molecule to produce adsorbed metal- CH_3 species [60,68–75], while in this study CH_4 can be easily activated by energetic electrons in plasma to produce CH_3 radicals instead of metal component, which also weakens the catalytic function of Au species.

Even so, by comparing the FTIR spectra of HZSM-5 and Au/HZSM-5 in Figure S6, it can be seen that loading Au on HZSM-5 enhances the intensity of adsorbed CO ($1800\text{--}2000\text{ cm}^{-1}$), but weakens the intensity of adsorbed HCO_3^- species, which indicates that the slight increase in acetic acid generation over Au/HZSM-5 might be related with the improved CO adsorption. Differently, loading Au on 13X enables FTIR bands disappeared at ca. 2170 and 2113 cm^{-1} , representing the CO interacting with Na^+ in 13X by C and O, respectively, but obviously enhances the formation of the carbonate-like specie ($-\text{CO}_3$) at 1707 cm^{-1} . These changes suggest that the improved acetic acid selectivity on Au/13X is probably attributed to the enhanced carbonate-like specie ($-\text{CO}_3$), originating from chemisorption of CO_2 on oxidized Au^{3+} species.

4. Conclusion

This work presents a strategy to tune the distribution of oxygenates in plasma-catalytic CH_4/CO_2 conversion over zeolite-based catalysts through the acidic sites, i.e., Brønsted acid site (BAS) and Lewis acid site (LAS). Results show that, the BAS in HZSM-5 significantly enhances the acetic acid generation, while the LAS in 13X favors alcohols production. These observed phenomena are explained by identifying active species both on surface and in plasma using *in-situ* FTIR and OES. On the HZSM-

5, the reaction pathways are dominated by CO_2 protonation on BAS with adsorbed bicarbonate as the key intermediate, followed by reacting with active CH_3 radicals in plasma through E-R mechanism, i.e., the bicarbonate pathway for the formation of acetic acid on BAS. Differently, on the 13X, H radical-assisted pathway leads to methanol generation through the adsorbed formate on LAS through E-R process. In addition, the corresponding Au/HZSM-5 and Au/13X catalysts were evaluated, and slightly positive effect of Au^{3+} on acetic acid production has been observed, which is probably related to the very low content and poor dispersion of Au species in the catalysts. Even so, Au^{3+} -BAS synergy still exhibits a potential for producing acetic acid. These fundamental insights obtained here provide a promising way for designing more-efficient bifunctional catalysts, to directly produce acetic acid or alcohols from CH_4 and CO_2 .

CRediT authorship contribution statement

Li Wang: Writing – review & editing, Writing – original draft, Software, Resources, Project administration, Methodology, Investigation, Formal analysis, Data curation, Conceptualization. **Yuezhao Wang:** Methodology, Formal analysis, Conceptualization. **Qian Chen:** Resources, Methodology. **Yimin Zhu:** Formal analysis, Data curation. **Yanhui Yi:** Resources, Formal analysis. **Linhui Fan:** Resources, Investigation, Conceptualization.

Declaration of Competing Interest

The authors declare that they have no known competing financial interests or personal relationships that could have appeared to influence the work reported in this paper.

Data Availability

Data will be made available on request.

Acknowledgements

We acknowledge financial support from the National Natural Science Foundation of China (22378037, 21908016), PetroChina Innovation Foundation (2019D-5007-0407) and the LiaoNing Revitalization Talents Program (XLYC1907008). Y.H. Yi acknowledges the funding from the National Natural Science Foundation of China [21503032, 22272015] and the Fundamental Research Funds for the Central Universities of China [DUT18JC42].

Appendix A. Supporting information

Supplementary data associated with this article can be found in the online version at doi:10.1016/j.apcatb.2024.123938.

References

- [1] W.C. Chung, M.B. Chang, Review of catalysis and plasma performance on dry reforming of CH_4 and possible synergistic effects, *Renew. Sust. Energ. Rev.* 62 (2016) 13–31.
- [2] Y. Diao, X. Zhang, Y. Liu, B. Chen, G. Wu, C. Shi, Plasma-assisted dry reforming of methane over $\text{Mo}_2\text{C-Ni}/\text{Al}_2\text{O}_3$ catalysts: Effects of $\beta\text{-Mo}_2\text{C}$ promoter, *Appl. Catal. B: Environ.* 301 (2022) 120779–120791.
- [3] Z. Sheng, H.H. Kim, S. Yao, T. Nozaki, Plasma-chemical promotion of catalysis for CH_4 dry reforming: unveiling plasma-enabled reaction mechanisms, *Phys. Chem. Chem. Phys.* 22 (2020) 19349–19358.
- [4] Y. Wang, L. Yao, S. Wang, D. Mao, C. Hu, Low-temperature catalytic CO_2 dry reforming of methane on Ni-based catalysts: A review, *Fuel Process. Technol.* 169 (2018) 199–206.
- [5] E.L. Saché, T.R. Reina, Analysis of Dry Reforming as direct route for gas phase CO_2 conversion. The past, the present and future of catalytic DRM technologies, *Prog. Energy Combust. Sci.* 89 (2022) 100970–101004.
- [6] A. Bogaerts, X. Tu, J.C. Whitehead, G. Centi, L. Lefferts, O. Guaitella, F.A. Jury, H. H. Kim, A.B. Murphy, W.F. Schneider, T. Nozaki, J. Chicks, A. Rousseau,

- F. Thevenet, A. Khacef, M. Carreon, The 2020 plasma catalysis roadmap, *J. Phys. D: Appl. Phys.* 53 (2020) 443001–443052.
- [7] A. George, B. Shen, M. Craven, Y. Wang, D. Kang, C. Wu, X. Tu, A review of non-thermal plasma technology: a novel solution for CO₂ conversion and utilization, *Renew. Sust. Energ. Rev.* 135 (2021) 109702–109723.
- [8] S. Liu, L.R. Winter, J.G. Chen, Review of plasma-assisted catalysis for selective generation of oxygenates from CO₂ and CH₄, *ACS Catal.* 10 (2020) 2855–2871.
- [9] H. Puliyalil, D.L. Jurković, V.D.B.C. Dasireddy, B. Likozar, A review of plasma-assisted catalytic conversion of gaseous carbon dioxide and methane into value-added platform chemicals and fuels, *RSC Adv.* 8 (2018) 27481–27508.
- [10] L. Wang, Y. Yi, C. Wu, H. Guo, X. Tu, One-Step Reforming of CO₂ and CH₄ into High-Value Liquid Chemicals and Fuels at Room Temperature by Plasma-Driven Catalysis, *Angew. Chem. Int. Ed.* 56 (2017) 13679–13683.
- [11] L. Yang, C.J. Liu, E. Baldur, Y. Wang, Synthesis of oxygenates and higher hydrocarbons directly from methane and carbon dioxide using dielectric-barrier discharges: product distribution, *Energy Fuel* 16 (2002) 864–870.
- [12] J.J. Zou, Y.P. Zhang, C.J. Liu, Y. Li, E. Baldur, Starch-enhanced synthesis of oxygenates from methane and carbon dioxide using dielectric-barrier discharges, *Plasma Chem. Plasma P.* 23 (2003) 69–82.
- [13] G. Scarduelli, G. Guella, D. Ascenzi, P. Tosi, Synthesis of liquid organic compounds from CH₄ and CO₂ in a dielectric barrier discharge operating at atmospheric pressure, *Plasma Process. Polym.* 8 (2011) 25–31.
- [14] L.M. Martini, G. Dilecce, G. Guella, A. Maranzana, G. Tonachini, P. Tosi, Oxidation of CH₄ by CO₂ in a dielectric barrier discharge, *Chem. Phys. Lett.* 593 (2014) 55–60.
- [15] M. Scapinello, L.M. Martini, P. Tosi, CO₂ hydrogenation by CH₄ in a dielectric barrier discharge: catalytic effects of Nickel and Copper, *Plasma Process. Polym.* 11 (2014) 624–628.
- [16] T. Kolb, J.H. Voigt, K.H. Gericke, Conversion of methane and carbon dioxide in a DBD reactor: influence of oxygen, *Plasma Chem. Plasma P.* 33 (2013) 631–646.
- [17] K. Krawczyk, M. Mlotek, B. Ulejczyk, K.S. Szalowski, Methane conversion with carbon dioxide in plasma-catalytic system, *Fuel* 117 (2014) 608–617.
- [18] A. Rahmani, M. Nikraveh, Impact of argon in reforming of (CH₄+CO₂) in surface dielectric barrier discharge reactor to produce syngas and liquid fuels, *Plasma Chem. Plasma P.* 38 (2018) 517–534.
- [19] M. Shirazi, E.C. Neyts, A. Bogaerts, DFT study of Ni-catalyzed plasma dry reforming of methane, *Appl. Catal. B: Environ.* 205 (2017) 605–614.
- [20] C. De Bie, J. van Dijk, A. Bogaerts, The dominant pathways for the conversion of methane into oxygenates and syngas in an atmospheric pressure dielectric barrier discharge, *J. Phys. Chem. C* 119 (2015) 22331–22350.
- [21] A.G. Ramirez, V.J. Rico, J. Cotrino, A.R.G. Elipe, R.M. Lambert, Low temperature production of formaldehyde from carbon dioxide and ethane by plasma-assisted catalysis in a ferroelectrically moderated dielectric barrier discharge reactor, *ACS Catal.* 4 (2013) 402–408.
- [22] A.N. Biswas, L.R. Winter, B. Loenders, Z.H. Xie, A. Bogaerts, J.G. Chen, Oxygenate production from plasma-activated reaction of CO₂ and ethane, *ACS Energy Lett.* 7 (2022) 236–241.
- [23] Y. Wang, Y. Chen, J. Harding, H. He, A. Bogaerts, X. Tu, Catalyst-free single-step plasma reforming of CH₄ and CO₂ to higher value oxygenates under ambient conditions, *Chem. Eng. J.* 450 (2022) 137860–137873.
- [24] D. Li, V. Rohani, F. Fabry, A.P. Ramaswamy, M. Sennour, L. Fulcheri, Direct conversion of CO₂ and CH₄ into liquid chemicals by plasma-catalysis, *Appl. Catal. B: Environ.* 261 (2020) 118228–118236.
- [25] J. Li, L. Dou, Y. Gao, X. Hei, F. Yu, T. Shao, Revealing the active sites of the structured Ni-based catalysts for one-step CO₂/CH₄ conversion into oxygenates by plasma-catalysis, *J. CO₂ Util.* 52 (2021) 101675–101699.
- [26] L. Dou, Y. Liu, Y. Gao, J. Li, X. Hu, S. Zhang, K. Ostrikov, T. Shao, Disentangling metallic cobalt sites and oxygen vacancy effects in synergistic plasma-catalytic CO₂/CH₄ conversion into oxygenates, *Appl. Catal. B: Environ.* 318 (2022) 121830–121842.
- [27] J. Li, L. Dou, Y. Liu, Y. Gao, Xi Hu, F. Yu, J. Li, S. Zhang, Tao Shao, One-step plasma reforming of CO₂ single bond CH₄ into hydrogen and liquid fuels: The roles of Cu and Fe sites on products distribution, *Fuel Process Technol.* 242 (2023) 107648–107662.
- [28] A. Wang, J.H. Harrhy, S. Meng, P. He, L. Liu, H. Song, Nonthermal plasma-catalytic conversion of biogas to liquid chemicals with low coke formation, *Energy Conv. Manag.* 191 (2019) 93–101.
- [29] M. Shirazi, E.C. Neyts, A. Bogaerts, DFT study of Ni-catalyzed plasma dry reforming of methane, *Appl. Catal. B: Environ.* 205 (2017) 605–614.
- [30] D. Mei, M. Sun, S. Liu, P. Zhang, Z. Fang, X. Tu, Plasma-enabled catalytic dry reforming of CH₄ into syngas, hydrocarbons and oxygenates: Insight into the active metals of γ -Al₂O₃ supported catalysts, *J. CO₂ Util.* 67 (2023) 102307–102318.
- [31] Y. Li, H. Yu, J. Dai, Z. Zhang, Z. Zhang, H. Yu, L. Liu, CH₄ and CO₂ conversion over boron nitride-supported Ni catalysts with B-O defects in DBD plasma, *Fuel Process. Technol.* 242 (2023) 107655–107668.
- [32] Y. Wang, L. Fan, H. Xu, X. Du, H. Xiao, J. Qian, Y. Zhu, X. Tu, L. Wang, Insight into the synthesis of alcohols and acids in plasma-driven conversion of CO₂ and CH₄ over copper-based catalysts, *Appl. Catal. B: Environ.* 315 (2022) 121583–121595.
- [33] L. Wang, Y. Wang, L. Fan, H. Xu, B. Liu, J. Zhang, Y. Zhu, X. Tu, Direct conversion of CH₄ and CO₂ to alcohols using plasma catalysis over Cu/Al(OH)₃ catalysts, *Chem. Eng. J.* 466 (2023) 143347–143360.
- [34] X. Yu, K. Hu, H. Zhang, G. He, Y. Xia, M. Deng, Y. Shi, C. Yang, X. Mao, Z. Wang, Plasma-Catalytic Ammonia Decomposition for Carbon-Free Hydrogen Production Using Low Pressure-Synthesized Mo₂N Catalyst, *Plasma Chem. Plasma P.* 43 (2023) 83–197.
- [35] Q. Chen, S. Meng, R. Liu, X. Zhai, X. Wang, L. Wang, H. Guo, Y. Yi, Plasma-catalytic CO₂ hydrogenation to methanol over CuO-MgO/Beta catalyst with high selectivity, *Appl. Catal. B: Environ.* 342 (2024) 123422–123434.
- [36] M. Ravi, V.L. Sushkevich, J.A.V. Bokhoven, Towards a better understanding of Lewis acidic aluminium in zeolites, *Nat. Mater.* 19 (2020) 1047–1056.
- [37] M. Choi, K. Na, J. Kim, Y. Sakamoto, O. Terasaki, R. Ryoo, Stable single-unit-cell nanosheets of zeolite MFI as active and long-lived catalysts, *Nature* 46 (2009) 246–249.
- [38] J. Holzinger, P. Beato, L.F. Lundegaard, J. Skibsted, Distribution of aluminum over the tetrahedral sites in ZSM-5 zeolites and their evolution after steam treatment, *J. Phys. Chem. C* 122 (2018) 15595–15613.
- [39] P. Lanzafame, K. Barbera, S. Perathoner, G. Centi, A. Aloise, M. Migliori, A. Macario, J.B. Nagy, G. Giordano, The role of acid sites induced by defects in the etherification of HMF on Silicalite-1 catalysts, *J. Catal.* 330 (2015) 558–568.
- [40] M. Thommes, K. Kaneko, A.V. Neimark, J.P. Olivier, F. Rodriguez-Reinoso, J. Rouquerol, K.S.W. Sing, Physisorption of gases, with special reference to the evaluation of surface area and pore size distribution (IUPAC Technical Report), *Pure Appl. Chem.* 87 (2015) 1051–1069.
- [41] Z.X. Yang, Y.D. Xia, R. Mokaya, Zeolite ZSM-5 with unique supermicropores synthesized using mesoporous carbon as a template, *Adv. Mater.* 16 (2004) 727–732.
- [42] M. Liu, G. Li, S. Zhang, X.H. Gao, B. Zhang, X.Y. Bai, H.T. Liu, H.H. Liu, Organic-free synthesis of hierarchical ZSM-5 via a combined strategy of unstable precursors and postsynthesis steam treatment, *Ind. Eng. Chem. Res.* 61 (2022) 6057–6064.
- [43] J.P. Marques, I. Gener, P. Ayraut, J.C. Bordado, J.M. Lopes, F. Ramôa Ribeiro, M. Guisnet, Infrared spectroscopic study of the acid properties of dealuminated BEA zeolites, *Microporous Mesoporous Mat.* 60 (2003) 251–262.
- [44] A. Redondo, P.J. Hay, Quantum chemical studies of acid sites in zeolite ZSM-5, *J. Phys. Chem.* 97 (1993) 11754–11761.
- [45] L.S.R. Silva, C.V.S. Almeida, C.T. Meneses, E.A. Batista, S.F. Santos, K.I.B. Eguiluz, G.R. Salazar-Banda, AuPd/C core-shell and alloy nanoparticles with enhanced catalytic activity toward the electro-oxidation of ethanol in alkaline media, *Appl. Catal. B: Environ.* 251 (2019) 313–325.
- [46] I. Tuzovskaya, N. Bogdanchikova, A. Simakov, V. Gurin, A. Pestryakov, M. Avalos, M.H. Farias, Structure and electronic states of gold species in mordenites, *Chem. Phys.* 338 (2007) 23–32.
- [47] D.B. Ingram, P. Christopher, J.L. Bauer, S. Linic, Predictive Model for the Design of Plasmonic Metal/Semiconductor Composite Photocatalysts, *ACS Catal.* 1 (2011) 1441–1447.
- [48] L. Wu, C.X. Qi, X. Sun, H.J. Su, L.B. Sun, L.J. Zhao, F.S. Xiao, A highly efficient bi-functional zeolite catalyst for low temperature catalytic cracking of n-octane to produce propylene: Joint contribution of nanogold and dealumination, *Appl. Catal. A Gen.* 646 (2022) 118862–118871.
- [49] M.M. Mohamed, T.M. Salama, R. Ohnishi, M. Ichikawa, Characterization of gold(I) in dealuminated H-Mordenite zeolite, *Langmuir* 17 (2001) 5678–5684.
- [50] Y.C. Chai, X. Han, W.Y. Li, S.S. Liu, S. Yao, C. Wang, W. Shi, I. da-Silva, P. Manuel, Y.Q. Cheng, L.D. Daemen, A.J. Ramirez-Cuesta, C.C. Tang, L. Jiang, S. Yang, N. J. Guan, L.D. Li, Control of zeolite pore interior for chemoselective alkyne/olefin separations, *Science* 368 (2020) 1002–1006.
- [51] K.C. Leung, S. Hong, G.C. Li, Y.D. Xing, B.K.Y. Ng, P.L. Ho, D.P. Ye, P. Zhao, E. Tan, O. Safonova, T.S. Wu, M.M.J. Li, G. Mpourmpakis, N.H. Tsang, Confined Ru sites in a 13X zeolite for ultrahigh H₂ production from NH₃ decomposition, *J. Am. Chem. Soc.* 145 (2023) 14548–14561.
- [52] N. Bouchoul, H. Touati, E. Fourré, J.-M. Clacens, I. Batonneau-Gener, C. Batiot-Dupeyrat, Plasma-catalysis coupling for CH₄ and CO₂ conversion over mesoporous macroporous Al₂O₃: Influence of the physico-chemical properties, *Appl. Catal. B: Environ.* 295 (2021) 120262–120270.
- [53] G. Busca, Acidity and basicity of zeolites: A fundamental approach, *Microporous Mesoporous Mat.* 254 (2017) 3–16.
- [54] A. Solis-Garcia, J.F. Louvier-Hernandez, A. Almendarez-Camarillo, J.C. Fierro-Gonzalez, Participation of surface bicarbonate, formate and methoxy species in the carbon dioxide methanation catalyzed by ZrO₂-supported Ni, *Appl. Catal. B: Environ.* 218 (2017) 611–620.
- [55] T. Montanari, E. Finocchio, E. Salvatore, G. Garuti, A. Giordano, C. Pistorino, G. Busca, CO₂ separation and landfill biogas upgrading: A comparison of 4A and 13X zeolite adsorbents, *Energy* 36 (2011) 314–319.
- [56] S. Coluccia, L. Marchese, G. Martra, Characterisation of microporous and mesoporous materials by the adsorption of molecular probes: FTIR and UV-Vis studies, *Microporous Mesoporous Mat.* 30 (1999) 43–56.
- [57] X.L. Wang, Y. Gao, S. Zhang, H. Sun, J. Li, T. Shao, Nanosecond pulsed plasma assisted dry reforming of CH₄: The effect of plasma operating parameters, *Appl. Energy* 243 (2019) 132–144.
- [58] C. De Bie, B. Verheyde, T. Martens, J. van Dijk, S. Paulussen, A. Bogaerts, Fluid Modeling of the Conversion of Methane into Higher Hydrocarbons in an Atmospheric Pressure Dielectric Barrier Discharge, *Plasma Process. Polym.* 8 (2011) 1033–1058.
- [59] Y. Du, K. Tamura, S. Moore, Z. Peng, T. Nozaki, P.J. Bruggeman, CO(B¹Σ⁺→A¹Π) Angstrom System for Gas Temperature Measurements in CO₂ Containing Plasmas, *Plasma Chem. Plasma Process.* 37 (2017) 29–41.
- [60] W. Panjan, J. Sirirajansre, C. Warakulwit, P. Pantu, J. Limtrakul, The conversion of CO₂ and CH₄ to acetic acid over the Au-exchanged ZSM-5 catalyst: a density functional theory study, *Phys. Chem. Chem. Phys.* 14 (2012) 16588–16594.
- [61] X.F. Wang, J.W. Jiang, Q.J. Xu, L.Y. Duan, H. Guo, Understanding inclusive quantum dots hollow CN@CIZS heterojunction for enhanced photocatalytic CO₂ reduction, *Appl. Surf. Sci.* 604 (2022) 154601–154609.

- [62] J.W. Jiang, X.F. Wang, Q.J. Xu, Z.Y. Mei, L.Y. Duan, H. Guo, Understanding dual-vacancy heterojunction for boosting photocatalytic CO₂ reduction with highly selective conversion to CH₄, *Appl. Catal. B: Environ.* 316 (2022) 121679–121689.
- [63] Q.J. Xu, J.W. Jiang, X.F. Wang, L.Y. Duan, H. Guo, Understanding oxygen vacant hollow structure CeO₂@In₂O₃ heterojunction to promote CO₂ reduction, *Rare Met* 42 (2023) 1888–1898.
- [64] J.W. Jiang, X.F. Wang, H. Guo, Enhanced Interfacial Charge Transfer/Separation By LSPR-Induced Defective Semiconductor Toward High CO₂RR Performance, *Small* 19 (2023) 2301280–2301289.
- [65] L. Wang, Y.H. Yi, Y.J. Guo, Y. Zhao, J.L. Zhang, H.C. Guo, Synergy of DBD plasma and Fe-based catalyst in NH₃ decomposition: enhancing adsorption step, *Plasma Process. Polym.* 14 (2017) e1600111–e16001117.
- [66] L. Wang, Y. Zhao, C.Y. Liu, W.M. Gong, H.C. Guo, Plasma driven ammonia decomposition on a Fe-catalyst: eliminating surface nitrogen poisoning, *Chem. Commun.* 49 (2013) 3787–3789.
- [67] Z.L. Cui, S.Y. Meng, Y.H. Yi, A. Jafarzadeh, S.K. Li, E.C. Neyts, Y.P. Hao, L.C. Li, X. X. Zhang, X.K. Wang, A. Bogaerts, Plasma-catalytic methanol synthesis from CO₂ hydrogenation over a supported Cu cluster catalyst: insights into the reaction, *ACS Catal.* 12 (2022) 1326–1337.
- [68] Y. Zhao, H. Wang, J. Han, X. Zhu, D. Mei, Q. Ge, Simultaneous activation of CH₄ and CO₂ for concerted C–C coupling at oxide–oxide interfaces, *ACS Catal.* 9 (2019) 3187–3197.
- [69] Y. Zhao, C. Cui, J. Han, H. Wang, X. Zhu, Q. Ge, Direct C–C coupling of CO₂ and the methyl group from CH₄ activation through facile insertion of CO₂ into Zn–CH₃ σ -bond, *J. Am. Chem. Soc.* 138 (2016) 10191–10198.
- [70] R. Shavi, J. Ko, A. Cho, J.W. Han, J.G. Seo, Mechanistic insight into the quantitative synthesis of acetic acid by direct conversion of CH₄ and CO₂: An experimental and theoretical approach, *Appl. Catal. B: Environ.* 229 (2018) 237–248.
- [71] X. Nie, X. Ren, C. Tu, C. Song, X. Guo, J.G. Chen, Computational and experimental identification of strong synergy of the Fe/ZnO catalyst in promoting acetic acid synthesis from CH₄ and CO₂, *Chem. Commun.* 56 (2020) 3983–3986.
- [72] J.F. Wu, S.M. Yu, W.D. Wang, Y.X. Fan, S. Bai, C.W. Zhang, Q. Gao, J. Huang, W. Wang, Mechanistic insight into the formation of acetic acid from the direct conversion of methane and carbon dioxide on zinc-modified H-ZSM-5 zeolite, *J. Am. Chem. Soc.* 135 (2013) 13567–13573.
- [73] B.D. Montejo-Valencia, Y.J. Pagán-Torres, M.M. Martínez-Iñesta, M.C. Curret-Arana, Density functional theory (DFT) study to unravel the catalytic properties of m-exchanged MFI, (M = Be, Co, Cu, Mg, Mn, Zn) for the conversion of methane and carbon dioxide to acetic acid, *ACS Catal.* 7 (2017) 6719–6728.
- [74] S. Wang, S. Guo, Y. Luo, Z. Qin, Y. Chen, M. Dong, J. Li, W. Fan, J. Wang, Direct synthesis of acetic acid from carbon dioxide and methane over Cu-modulated BEA, MFI, MOR and TON zeolites: a density functional theory study, *Catal. Sci. Technol.* 9 (2019) 6613–6626.
- [75] A.M. Rabie, M.A. Betiha, S.E. Park, Direct synthesis of acetic acid by simultaneous co-activation of methane and CO₂ over Cu-exchanged ZSM-5 catalysts, *Appl. Catal. B: Environ.* 215 (2017) 50–59.